Tectonics

RESEARCH ARTICLE
10.1029/2021TC006699

Key Points:

- Activity along the shear zone exhuming Cer metamorphic core complex in the internal Dinarides was dated by $^{40}Ar/^{39}Ar$ geochronology to ~17 Ma
- Exhumation was facilitated by extensional reactivation of Late Cretaceous-Paleogene nappe contacts resulting from Adria-Europe collision
- Extensional reactivation of the thrusts is interpreted as a far-field effect of Oligo-Miocene Carpathian slab rollback

Supporting Information:

Supporting Information may be found in the online version of this article.

Correspondence to:

G. Löwe,
georg.loewe@uni-jena.de

Citation:

Löwe, G., Schneider, S., Sperner, B., Balling, P., Pfänder, J. A., & Ustaszewski, K. (2021). Torn between two plates: Exhumation of the Cer massif (internal Dinarides) as a far-field effect of Carpathian slab rollback inferred from $^{40}Ar/^{39}Ar$ dating and cross section balancing. *Tectonics*, *40*, e2021TC006699. https://doi.org/10.1029/2021TC006699

Received 6 JAN 2021
Accepted 16 MAY 2021

Torn Between Two Plates: Exhumation of the Cer Massif (Internal Dinarides) as a Far-Field Effect of Carpathian Slab Rollback Inferred From $^{40}Ar/^{39}Ar$ Dating and Cross Section Balancing

Georg Löwe[1], Susanne Schneider[2], Blanka Sperner[2], Philipp Balling[1], Jörg A. Pfänder[2], and Kamil Ustaszewski[1]

[1]Institut für Geowissenschaften, Friedrich-Schiller-Universität Jena, Jena, Germany, [2]Institut für Geologie, TU Bergakademie Freiberg, Freiberg, Germany

Abstract Extension across the southern Pannonian Basin and the internal Dinarides is characterized by Oligo-Miocene metamorphic core complexes (MCCs) exhumed along mylonitic low-angle extensional shear zones. Cer MCC at the transition between Dinarides and Pannonian Basin occupies a structural position within the distal-most Adriatic thrust sheet and originates from two different tectonic processes: Late Cretaceous-Paleogene nappe-stacking during a continent-continent collision with Adria in a lower plate position, and exhumation related to Miocene extension driven by the Carpathian slab-rollback. Structural data and a balanced cross section across the Cer massif show linking of the exhuming shear zone to a breakaway fault, which reactivated the early Late Cretaceous most internal nappe contact. Paleozoic greenschist-to amphibolite-grade lithologies surround a polyphase intrusion composed of I- and S-type granites and were exhumed along a shear zone characterized by top-N transport. Thermobarometric analyses indicate an intrusion depth of 7–8 km of the Oligocene I-type granite; cooling below ~500°C occurred at 25.4 ± 0.6 Ma (1σ) yielded by $^{40}Ar/^{39}Ar$ dating of hornblende. Biotite and white mica from this intrusion as well as from the mylonitic shear zone yield $^{40}Ar/^{39}Ar$ cooling ages of 17–18 Ma independent of the used techniques (in situ laser ablation, single-grain total fusion, single-grain step heating, and multi-grain step heating). White mica from the S-type granite yield an $^{40}Ar/^{39}Ar$ cooling age of 16.7 ± 0.1 Ma (1σ). Associated dikes intruding the shear zone were also affected by N-S extension resulting in the exhumation of the MCC, which was triggered by the opening of the Pannonian back-arc basin in response to the Carpathian slab-rollback.

Plain Language Summary Horizontal stretching of continental plates induces thinning of the crustal upper part, melting of rocks, the sinking of the land surface, and formation of large basins. One of the world's best-studied basins formed by such a process is the Central European Pannonian Basin. This basin is surrounded by the mountain belts of the Alps, Carpathians, and Dinarides. We have studied rocks between the Pannonian Basin and the southerly adjacent Dinaride Mountains, where rocks deposited in the basin are found right next to rocks that were initially about 7–8 km deep in the crust. These rocks are separated by a shear zone, along which they were brought to the surface. We have dated the activity of the shear zone by measuring concentrations of radioactive isotopes and their decay products contained in deformed minerals. The shear zone was active at a time when the Pannonian Basin started to open due to tectonic processes further NE underneath the Carpathian mountain chain. We also found evidence that the shear zone, which brought metamorphic rocks upwards was formerly one that brought rocks downwards into the crust during an earlier phase of mountain building, predating basin formation.

1. Introduction

Back-arc extension due to slab-rollback (Uyeda & Kanamori, 1979) is often observed in the hinterland of convergent plate boundaries and promotes the formation of large rift basins (Malinverno & Ryan, 1986). One of the largest continental back-arc basins in the circum-Mediterranean region is the Pannonian Basin (Figure 1), which formed in Late Oligocene to Late Miocene times in response to slab-retreat underneath the Carpathian orogen (e.g., Horvath & Berckhemer, 1982; Horváth et al., 2006; Royden, 1988; Royden

10.1029/2021TC006699

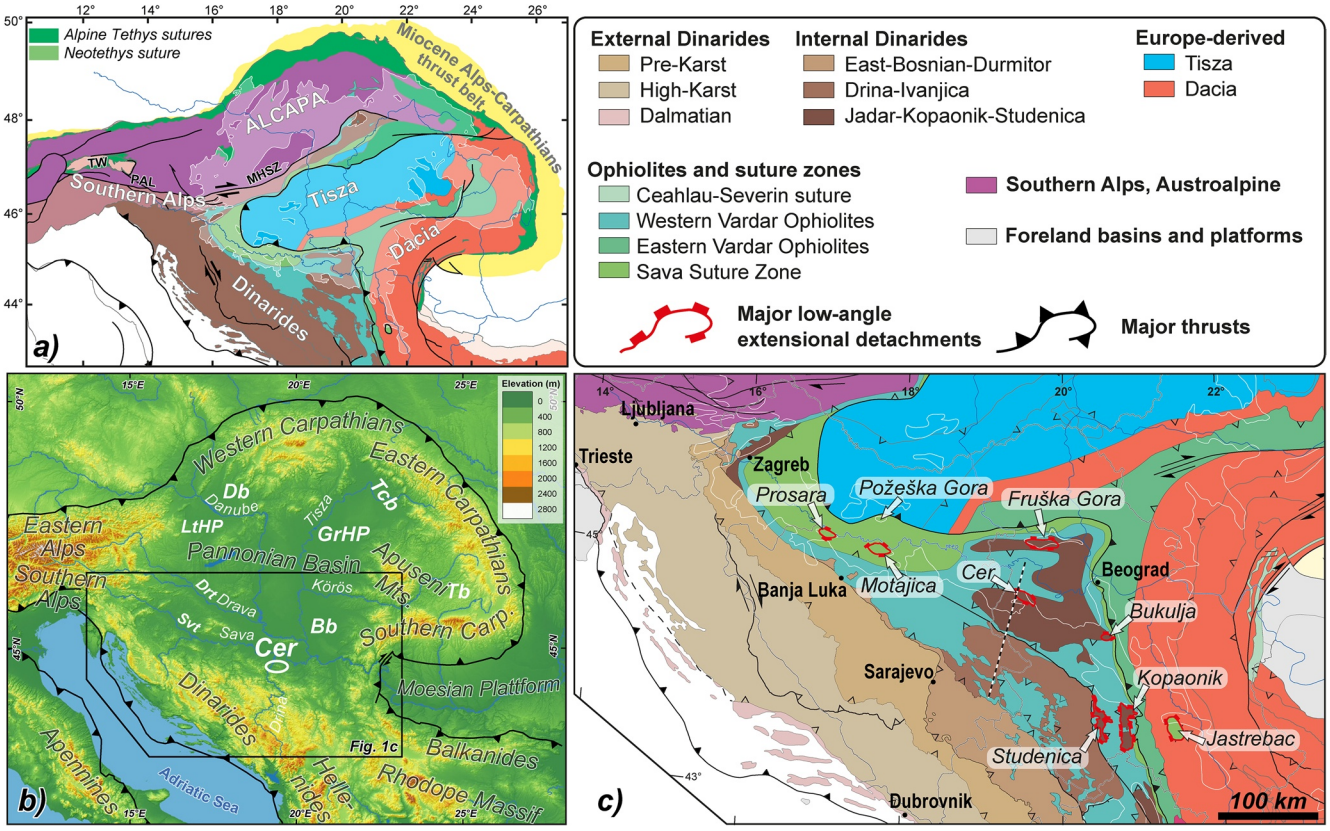

Figure 1. (a) Simplified overview map of major tectonic units and fault zones of the Alps-Carpathians-Dinarides region (modified after Schmid et al., 2020). MHSZ, Mid-Hungarian shear zone; PAL, Periadriatic line; TW, Tauern window. Shaded area depicts the extent of the Pannonian Basin. (b) Digital Elevation map (based on SRTM data with 90 m resolution) of the Pannonian Basin and surrounding orogens with their respective deformation fronts. Abbreviations (white bold italic) indicate major subbasins of the Pannonian Basin system: Bb, Banat Basin; Db, Danube basin; Drt, Drava trough; GrHP, Great Hungarian Plain; LtHP, Little Hungarian Plain; Svt, Sava trough; Tb, Transylvanian basin; Tcb, Transcarpathian basin. (c) Tectonic units of the Dinarides and neighboring regions (modified after Schmid et al., 2020) with locations of metamorphic core complexes and associated low-angle detachment faults in red. The dashed line depicts the location of the cross section trace (Figure 12).

et al., 1983). The basin hosts up to 7 km thick sedimentary successions (Nemcok et al., 1998) and sub-surface data suggest E-W- to NE-SW-directed extension (e.g., Fodor et al., 1999), triggering exhumation of several metamorphic core complexes (MCCs) along low-angle detachment faults (e.g., Lister & Davis, 1989) that separate Miocene strata from the Paleozoic basement (Tari & Pamić, 1998). In the central Pannonian Basin, these MCCs remain subsurface due to substantial Late Miocene post-rift subsidence (e.g., Balázs et al., 2016; Tari et al., 1999). By contrast, the southwestern margin of the Pannonian Basin at the transition into the structurally underlying, but topographically more prominent internal Dinarides hosts a chain of several exposed MCCs accessible for field studies. These exposed MCCs provide insight into the kinematics and timing of extensional processes that operated during the opening of the Pannonian Basin system (Figure 1).

Oligo-Miocene extension across the Pannonian Basin system involved the extensional reactivation of earlier contractional faults (e.g., Horváth, 1993; Tari et al., 1992). This includes the reactivation of Maastrichtian suturing thrusts between Europe- and Adria-derived units along the southern margin with the Dinarides fold-thrust belt (Ustaszewski et al., 2010), as well as segments of this suture zone against the Carpatho-Balkan orogen further south (Erak et al., 2017; Matenco & Radivojević, 2012). Extensional reactivation of large-scale thrusts is not uncommon and has been reported from various other collisional orogens like the Grenville orogen (Busch et al., 1997), the Caledonides (Fossen, 1992), or the Eastern Alps (Froitzheim et al., 1997). The existence of extensionally reactivated large-scale thrusts in the hinterland of the Dinaric orogen, however, is still speculative.

In this study, we present geochronological data obtained by $^{40}Ar/^{39}Ar$ in situ-, multi- and single-grain step-heating and single-grain total fusion techniques on mica and amphibole from a low-angle mylonitic shear zone and the undeformed footwall in the Cer Massif (central western Serbia; Figures 1b and 1c). We chose this multi-technique approach to (a) constrain the cooling history of the Cer Massif, (b) combine the advantages of each technique in order to gain unambiguous information about shear zone activity, and (c) evaluate individual results with regard to their internal consistency.

The results help us to understand the kinematics and timing of extension responsible for the formation of a MCC located at the transition between the two most internal Adria-derived thrust sheets of the internal Dinarides, namely the Drina-Ivanjica- and Jadar-Kopaonik nappes. Building on our observations, we suggest that larger parts of the internal Dinarides underwent large-scale early Neogene extension by reactivation of nappe contacts and show that the amount of extension increased from the external across the internal Dinarides toward the Pannonian Basin.

2. Geological Overview

The geodynamic evolution of central eastern Europe resulted in the formation and closure of several oceanic basins. During the Middle Triassic, rifting led to the opening of the Neotethys Ocean. After the obduction of the Western Vardar ophiolites onto the passive Adriatic margin in the Kimmeridgian (e.g., Gawlick & Missoni, 2019; Robertson et al., 2009), progressive convergence led to continued northeastward subduction of the northern branch of the Neotethys (Gallhofer et al., 2015, 2017). Continent-continent collision in latest Cretaceous-to Paleogene times (e.g., Pamić et al., 2002; Ustaszewski et al., 2009) culminated in the formation of the Dinarides fold-and-thrust belt (Figures 1a and 1b) and involved Adria-derived thrust sheets in a lower plate position and blocks of European affinity, i.e., Tisza and Dacia mega-units, which separated from the European plate in the Late Triassic (Haas & Péró, 2004) in the upper plate, above the oceanic suture. For the sake of simplicity, we will refer to these mega-units as "European plate."

The Dinarides are commonly divided into internal and external Dinarides. The external Dinarides consist of nappes derived from the Adriatic Carbonate Platform, while the internal Dinarides comprise a number of so-called "composite nappes," which are composed of distal Adriatic continental units that carry the obducted ophiolites of the Western Vardar unit, with the obduction interface dissected by Late Cretaceous west-to southwest-vergent thrusts (Schmid et al., 2020; Vlahović et al., 2005).

The Jadar-Kopaonik composite nappe (Figure 1c) encompasses deformed Middle Devonian to Carboniferous turbiditic sequences overlain by Permian to Upper Jurassic limestones (Filipović et al., 2003) and was thrust onto the Drina-Ivanjica composite nappe (Figure 1c), which contains Paleozoic basement mainly composed of Carboniferous metasandstones, metaconglomerates, metapelites and marble that experienced anchizonal metamorphism during WNW-directed obduction of the Western Vardar ophiolites (Brković et al., 1977; Porkoláb et al., 2019). The lowermost nappe of the internal Dinarides is the East-Bosnian-Durmitor composite nappe (Figure 1c), which structurally underlies the Drina-Ivanica thrust sheet. These composite nappes formed by out-of-sequence thrusting, with respect to the Late Jurassic obduction, during ongoing Late Cretaceous to Early Paleogene shortening (Figure 1c; Schmid et al., 2020). Our study area in the internal Dinarides encompasses the most distal composite nappes, namely the Drina-Ivanjica and Jadar-Kopaonik thrust sheets, which are exposed as tectonic windows below the obducted Western Vardar ophiolites (Figure 1c) and structurally underlie the suture that separates the Adriatic lower plate from the upper European plate (Figure 1c). This suture zone was first described as the Vardar-Zone by Kossmat (1924) in southern Serbia, Macedonia, and northern Greece. Subsequent studies (Pamić, 1993) extended the zone NNW-ward until Beograd, where it forms a wide E-W-striking corridor, broadly following the course of the Sava River to Zagreb (Figure 1). Following Schmid et al. (2008), we will refer to it as the "Sava suture zone." The Sava suture zone represents an accretionary prism that primarily consists of Late Cretaceous trench-fill sediments and subordinate ophiolite-bearing units (Ustaszewski et al., 2009, 2010) and is in part covered by Neogene sediments of the Pannonian Basin (Figure 1c).

The Pannonian Basin is surrounded by the mountain belts of the Alps, Carpathians, and Dinarides and extends across the Sava suture zone in the south (Figures 1a and 1b). It covers numerous tectonic units of different origin, namely the ALCAPA block, the Tisza- and Dacia mega units, parts of the Southern

Alps, and the internal Dinarides (Figure 1a). The ALCAPA block comprises units of the Alps, Carpathians, and the Pannonian realm (Austroalpine and inner/central West Carpathian units) and is bound to the north by a complex suture zone of the Alpine Tethys and by the Periadriatic Fault system and its eastward extension into the Mid-Hungarian Shear Zone in the south (Figure 1a). The Tisza- and Dacia blocks represent two crustal fragments of European affinity located south of the ALCAPA terrane. Convergence between the European foreland in the northeast and the ALCAPA- and Tisza-Dacia blocks were followed by a Middle Miocene collision first in the Western Carpathians when buoyant continental crust entered the subduction channel (Sperner et al., 2002). This Neogene "soft" collision (Balla, 1987) between ALCAPA and the Tisza-Dacia mega-units with the European foreland resulted in the formation of the Carpathian orogen (Schmid et al., 2008). Roll-back of the European lithospheric slab beneath the Carpathian arc (Bada et al., 1999; Fodor et al., 1999; Horváth et al., 2006; Royden, 1988; Royden et al., 1983) was associated with the large-scale lithospheric extension of the upper plate formed by the ALCAPA- and Tisza-Dacia blocks during Early Miocene times, leading to the formation of the Pannonian rift basin.

The contemporaneous northward indentation of the Adriatic lithosphere toward Europe led to lateral extrusion of the Eastern Alps into the Pannonian rift basin (Ratschbacher et al., 1991; Rosenberg et al., 2004). Collision of ALCAPA and Tisza-Dacia with the European foreland migrated along-strike the Carpathian arc, followed by slab detachment in the Western Carpathians at 16 Ma, while subduction in the Eastern Carpathians was still ongoing at 13 Ma (Sperner et al., 2002; Tomek & Hall, 1993). E-ward slab retreat and subsequent break-off migrated toward the Eastern Carpathians, associated with E-W extension in the Pannonian Basin. Extension of the lithosphere in the Pannonian Basin was concurrent with the upwelling of the asthenosphere and led to an elevated heat flow (Dovenyi & Horváth, 1988; Horváth et al., 2015; Royden et al., 1983). The extension was accommodated by the formation of horst-graben structures (e.g., Sava- and Drava trough, Figure 1b; Tari & Pamić, 1998) and along low-angle normal faults that exhumed high-grade metamorphic rocks in the footwall, for instance in the Little- and Great Hungarian Plains (Figure 1b; Tari et al., 1992).

2.1. Core Complexes in the Internal Dinarides

A chain of Oligo-Miocene MCCs is exposed along the Sava suture zone and within the nappes of the internal Dinarides (e.g., Pamić et al., 2002; Schefer et al., 2011). Most of these core complexes are associated with magmatic activity and therefore contain intrusions. The S-type intrusion of the Motajica MCC (Figure 1c) intruded the Sava suture zone at c. 27 Ma and was exhumed with a framework of upper greenschist-to upper amphibolite-grade rocks. The exhumation took place along former latest Cretaceous suturing thrusts, which were extensionally reactivated as low-angle shear zones during E-W extension in the latest Oligocene-to early Miocene times (Ustaszewski et al., 2010). Extensional unroofing started at ~25 Ma and was followed by synrift sedimentation in the Sava trough (Figure 1b) during Ottnangian to Badenian times (Central Paratethys stages, corresponding to ~18.2–12.7 Ma; Harzhauser and Piller [2007]), linking this phase of the extension to the Neogene opening of the Pannonian back-arc basin system (Ustaszewski et al. (2010). Further east, the Bukulja MCC, which contains a large multiphase intrusion comprising two-mica granites and hornblende-biotite granites (Figure 1c) was exhumed along a low-angle detachment with top-E transport. Results of low-temperature thermochronology constrained the timing of rapid cooling associated with tectonic exhumation to late Middle Miocene times (14–11 Ma, Stojadinovic et al., 2013).

Another group of MCCs is situated in the Kopaonik-Studenica region (Figure 1c), also within the Jadar-Kopaonik composite nappe. The Kopaonik- and Studenica core complexes are composed of Paleozoic metasediments metamorphosed during greenschist-to amphibolite-facies conditions that contain Oligocene I-type- and Miocene S-type granites (Schefer et al., 2011), similar to Cer MCC. The intrusion of S-type granites at 17.7–18.1 Ma were contemporaneous to N-S-directed extension and subsequent core-complex formation during exhumation (Schefer et al., 2011).

2.2. Cer Metamorphic Core Complex

Cer MCC is located in central western Serbia and hosts a multi-phase pluton that intruded into the Paleozoic basement of the Jadar-Kopaonik thrust sheet (Figures 1c and 2), which comprises a suite of alternating

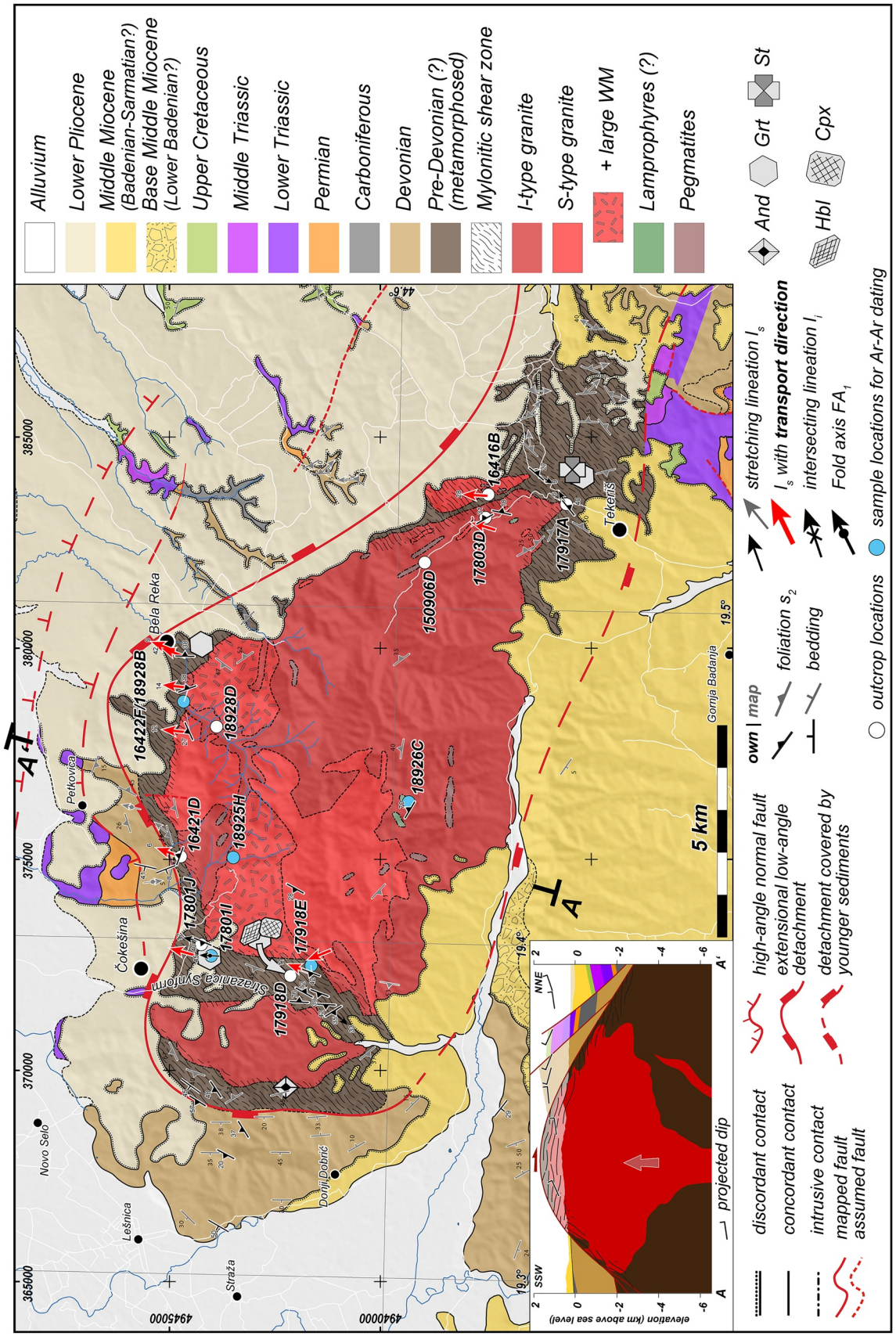

Figure 2. Geological map of Cer metamorphic core complex (MCC) based on the Yugoslavian map sheets "Zvornik" and "Vladimirci," 1:100000 (WGS84, UTM Zone 34N, Filipović (1971); Mojsilović et al. (1975)), supplemented by own observations. Gray structural elements are adopted from the Yugoslavian maps. Inset: Schematic cross-section along a N-S-profile through Cer MCC (for a regionally larger version see Figure 13). The bold red line represents the low-angle extensional detachment with top-N transport.

metapsammites and–pelites that experienced contact metamorphism and were exhumed along an extensional mylonitic shear zone (Stojadinovic et al., 2017). The pluton comprises a locally amphibole-bearing I-type Qz-monzonite to Qz-monzodiorite, subsequently intruded by a peraluminous S-type granite (Cvetković et al., 2007; Knezevic et al., 1994; Koroneos et al., 2011). The I-type intrusion hosts mafic enclaves with Hbl, Bt and Pl as main constituents (Knežević et al., 1994; Koroneos et al., 2011). West of the main intrusion a plutonic body of Qz-monzonitic composition termed *Stražanica intrusion* is exposed. To the south, the Cer MCC is discordantly overlain by gently south-dipping Miocene strata comprising alternations of marine to lacustrine conglomerates, sandstones, and shales. The basal parts of this succession crop out in close vicinity of the Cer MCC and rework igneous and metamorphosed rocks (Figure 2). The age of this succession corresponds to lower Badenian to Sarmatian(?) (~16–12 Ma), according to the Paratethys stages of Harzhauser and Piller (2007). The Cer MCC is discordantly overlain by Pliocene strata to the north. The Paleozoic rocks surrounding the pluton display a contact metamorphic overprint that reaches upper greenschist-to amphibolite-facies indicated by garnet- and staurolite-bearing mica schists. Other lithologies include phyllites, chlorite- and sericite-chlorite schists (Koroneos, et al., 2011). U-Pb (Zrn) ages of the I-type intrusion constrain crystallization to Early Oligocene times (31.36 ± 0.49 Ma to 32.21 ± 0.30 Ma; Stojadinovic et al., 2017). K-Ar cooling ages from white mica of the S-type granite range between 15.96 ± 0.64 Ma and 16.48 ± 0.65 Ma, while feldspar yielded ages of 15.10 ± 0.58 Ma and 15.20 ± 0.60 Ma (Koroneos et al., 2011). Both magmatic suites seem to be genetically linked to the intrusives at Bukulja (Cvetković et al., 2007).

3. Methods

To investigate the polyphase deformation history of the Cer MCC we combined thermobarometric calculations on the I-type intrusion, $^{40}Ar/^{39}Ar$ geochronology of deformed rocks of the exhuming shear zone as well as undeformed rocks of the footwall. Additionally, cross section balancing helped to quantify the amount of shortening and subsequent extension across the Jadar-Kopaonik thrust sheet.

3.1. Electron Microprobe Analyses

Analyses of major element concentrations on amphiboles of the I-type intrusion were carried out on a JEOL JXA-8230 electron microprobe at Jena University. The operating conditions were set to an accelerating voltage of 15 kV, a beam current of 5 nA, and a beam diameter between 1 and 5 μm. The wavelength-dispersive X-ray spectrometers were used to measure the elements and X-ray lines of Si, Ti, Al, Mn, Ca, Na, K, F, and Fe. Concentrations of element oxides were then used for thermobarometry after Ridolfi and Renzulli (2012). This thermobarometer is based on the aluminum content of magmatic calcic amphiboles and calibrated for X (Mg/Mg + Fe) ratios of >0.5.

3.2. $^{40}Ar/^{39}Ar$ Geochronology

All Ar isotopic analyses were carried out at the Argon Lab Freiberg (ALF, TU Bergakademie Freiberg). Irradiation was done at the LVR-15 research reactor of the Nuclear Research Institute in Řež, Czech Republic. An internal standard (Drachenfels sanidine DRF1) with an age of 25.682 ± 0.030 Ma was used as a fluence monitor during irradiation. The DRF1 monitor age is calibrated against Fish Canyon sanidine with 28.305 ± 0.036 Ma and using a decay constant of $\lambda = 5.5492 \times 10^{-10}$ (Renne et al., 2010) and an atmospheric $^{40}Ar/^{36}Ar$ ratio of 298.6 ± 0.3 (Lee et al., 2006). A GV Instruments ARGUS noble gas mass spectrometer equipped with five Faraday cups for static Ar isotope analysis was used in combination with a New Wave 30W floating CO_2 laser system and a Createc furnace system for multi-grain step heating analyses (for details see Pfänder et al., 2014). Gas purification prior to measurement was achieved by two SAES GP50 getter pumps, one operating at room temperature, the other at 400°C. A Thermo Scientific ARGUS VI noble gas mass spectrometer with five Faraday cups and a CDD electron multiplier at the L3 low mass side as well as with deflection dynodes on all mass positions for multi-dynamic measurements was used in combination with an ArF Teledyne Photon Machines Analyte Excite 193 nm laser for in situ analyses. Multiple single grain total fusion analyses on grain size fractions 80–250 μm, 250–500 μm, 500–1000 μm and 1–2 mm were carried out on the same mass spectrometer adopting an in-house build 25W Synrad CO_2 laser system in combination with a Raylase scanhead for beam deflection. Intercept calculation and raw data reduction

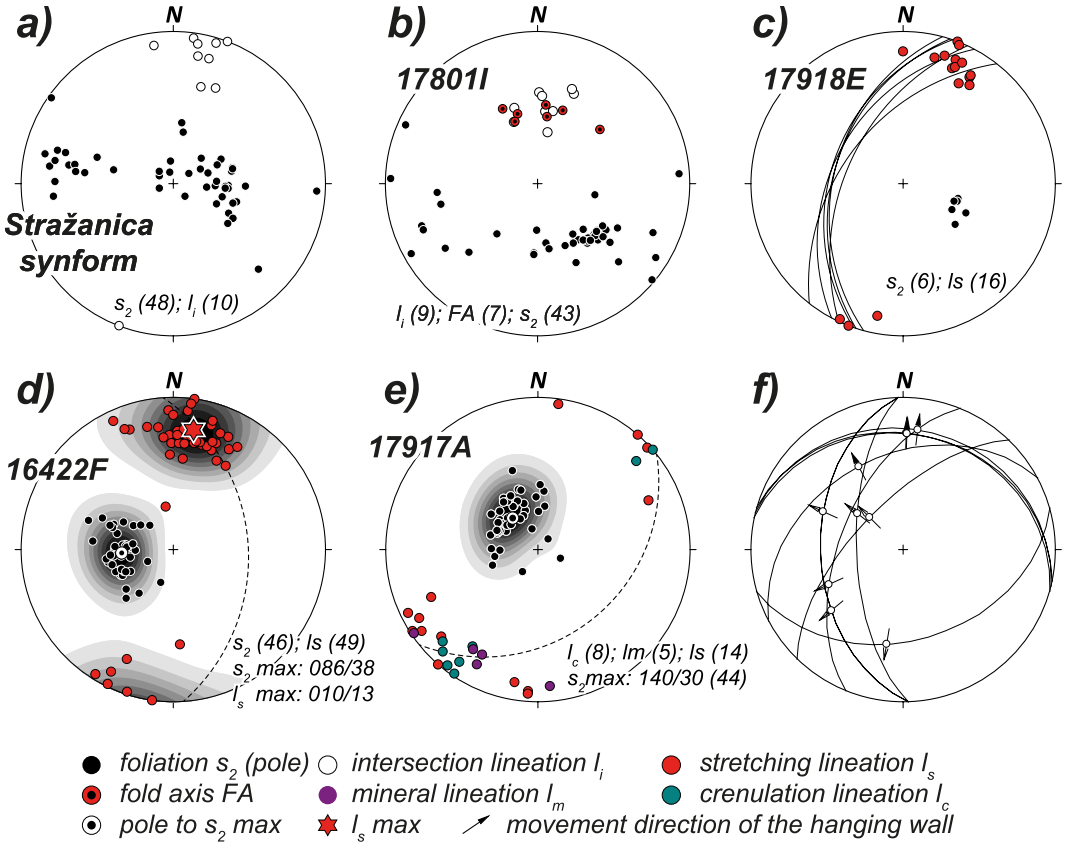

Figure 3. Stereographic projections (equal area, lower hemisphere) of structural data from various parts of the Cer MCC: (a) mylonitic shear zone within the central Stražanica synform; (b) northern Stražanica synform; (c) S-type granite at the eastern limb of the Stražanica synform with kinematic indicators showing top-N transport; (d) mylonites at the northeastern margin of Cer MCC; (e) structural data collected north of Tekeriš; (f) brittle fault planes with slip lineations from the magmatic core of Cer MCC.

were performed using an in-house developed Matlab software. Details regarding sample treatment, sample preparation, measurement protocol, and data evaluation are described in the supplement. For calculation of inverse isochron ages, weighted mean ages (WMA), and data visualization the R package *IsoplotR* was used (Vermeesch, 2018).

3.3. Cross Section Balancing

Cross-section construction was based on a compilation of former Yugoslavian geological maps of the Federal Geological Survey, Beograd, and available stratigraphic data of the Jadar-Kopaonik- and Drina-Ivanjica thrust sheets (Filipović, 1971; Mojsilović et al., 1975; Rajčević, 1982; Vrhovčić et al., 1984). Projected seismic profiles (Matenco & Radivojević, 2012), field observations, and results from thermobarometric analyses (see Section 4.3) were considered. Based on these data, a deformed-state cross-section was constructed first. Thicknesses of individual stratigraphic units were estimated based on dip data and lithological contacts. Retro-deformation of the cross-section was accomplished by using the fault bend fold (Suppe, 1983) and fault parallel flow (Egan et al., 1997) algorithms for the contractional stages, as well as the simple shear algorithm (Gibbs, 1983; Withjack & Peterson, 1993) for the extensional stages. Fault geometries and displacement amounts were constrained by iterative forwarding- and retro-deformation steps. This modeling approach resulted in a best fit model that provided geometry and depth for faults associated with nappe stacking and subsequent extension.

4. Results

4.1. Field Observations and Structural Data

Bedding planes within the unmetamorphosed Paleozoic basement are dominantly west-to north-west-dipping and developed a layer-parallel cleavage s_1. Cleavage s_1 is only observed locally, as it is folded and overprinted by an axial-planar cleavage s_2, which becomes densely spaced with increasing proximity to the pluton. This main metamorphic foliation always dips away from the pluton and envelopes it concentrically. Cleavage s_2 contains stretching lineations (Figures 3c–3e) associated with top-N transport and becomes mylonitic close to the contact with the pluton as strain increases, resulting in a decameter-scale ductile shear zone. The Paleozoic basement rocks are fault-bound against a succession of dark, organic-rich Permian limestones and light gray Triassic limestones in the north of Cer, which are discordantly overlain by Cretaceous carbonates in the northeast (Figure 2).

The Paleozoic metasediments surrounding the pluton experienced metamorphism reaching amphibolite-facies conditions with garnet-staurolite schists outcropping south-east of the pluton (Figures 2 and 4b), which display a SE-dipping main foliation with NE- and SW-plunging lineations (Figure 3e) and garnet-mica schists at the north-western margin of Cer MCC (Figures 4b and 4c, Table 1). Brittle striated faults cross-cut the metamorphic foliation and indicate multidirectional extension (Figure 3f).

Andalusite-bearing schists crop out at the western margin of the Stražanica intrusion, which is separated from the main intrusion by an N-S striking synform, hereafter termed *Stražanica synform* (Figures 2 and 4l). The synform hosts mylonitized garnet- and pyroxene-bearing hornblende-hornfels at the eastern limb (Figures 2 and 4g). The northern part hosts garnet-bearing mica schists, that partially preserved relics of s_1 (Figures 4e and 4f). Small scale minor folds of more competent layers in this area are characterized by N-plunging fold-axes (Figure 3b). The deformed parts of the main intrusion exhibit a s_2 foliation associated with pervasive S-C- and C′-fabrics that indicate top-N transport (Figures 4h and 4i). Close to the contact between the Stražanica synform and the main intrusion (outcrop 17918E; Figure 2), subhorizontal NNE- and SSW-plunging stretching lineations (Figure 3c) developed in an S-type granitic gneiss and are associated with top-NNE transport. The mylonite zone becomes more pronounced in the northeast, characterized by an E-dipping compositional layering with NNE-plunging stretching lineations, associated with NNE-directed transport (Figure 3d). Here, a migmatitic section of the shear zone is exposed (Figure 2; outcrop 16,422F/18928B; Figure 5).

4.2. Petrography and Microstructures

4.2.1. Magmatic Rocks

I-type intrusion: The I-type intrusion of Cer MCC consist of *Qz* + *Pl* + *Kfs* + *Bt* ± *Hbl* ± *Ttn* ± *Ilm* (Figure 4n) and varies in composition from Qz-monzonitic to Qz-monzodioritic (Koroneos et al., 2011). It will be summarized as Qz-monzodioritic in the following. The margin of the intrusion is overprinted by the shear zone (hatched signature in Figure 2), forming a solid-state foliation, which is mainly defined by biotite and developed top-N extensional C′-type shear bands (Figure 4h). Dynamic recrystallization by subgrain rotation (SGR) and grain boundary migration (GBM) of quartz and rotation of feldspar clasts as well as deformation twinning of plagioclase was observed.

S-type granite: The S-type granite consists of Qz + *Kfs* + *Pl* + *Wm* ± *Grt* ± *Trm* with garnet as a magmatic phase (Figure 4o). In parts, the S-type granite hosts up to cm-large blasts of white mica. The S-type granite occurs as either larger bodies or as dikes that cross-cut the I-type Qz-monzodiorite and thus are related to a younger magmatic event. The dikes can develop different grain sizes ranging from aplitic to pegmatitic, with feldspar- and white mica crystals several cm in size. They are always associated with magmatic garnet. The dikes intruding the shear zone were subsequently deformed which manifests in the field as asymmetric boudinage, and in thin sections as mica fish, dynamic recrystallization of quartz by SGR/GBM and C′-type shear bands indicating top-N transport (Figure 6).

In areas where the intrusion is affected by the shear zone, the S-type granite is characterized by a spaced foliation resulting in a gneissic structure (Figure 4i). Quartz shows dynamic recrystallization by SGR and

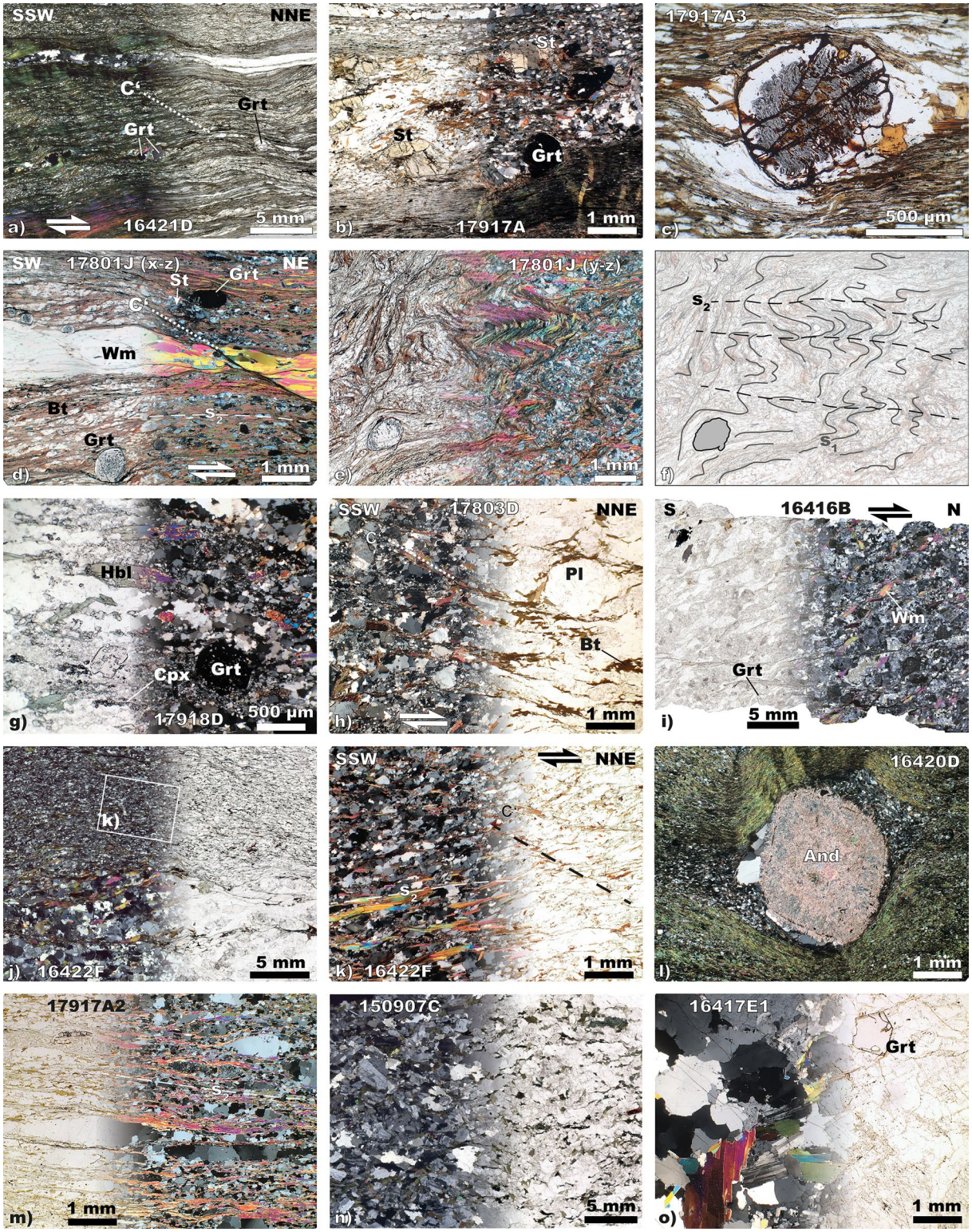
SSW
NNE
C'
Grt
Grt
a)
16421D
5 mm
St
St
Grt
b)
17917A
1 mm
17917A3
c)
500 µm
SW
17801J (x-z)
NE
St
Grt
C'
Wm
Bt
S_2
Grt
d)
1 mm
17801J (y-z)
e)
1 mm
S_2
S_1
f)
Hbl
Cpx
Grt
g)
17918D
500 µm
SSW
17803D
NNE
C'
Pl
Bt
h)
1 mm
S
16416B
N
Wm
Grt
i)
5 mm
k)
j)
16422F
5 mm
SSW
NNE
C'
S_2
k)
16422F
1 mm
16420D
And
l)
1 mm
17917A2
S
m)
1 mm
150907C
n)
5 mm
16417E1
Grt
o)
1 mm

GBM. White mica forms mica fish and forms part of C′-type shear bands (Figure 4i), indicating top-N transport.

Migmatites: These only sporadically exposed migmatitic rocks crop out near the village of Bela Reka (Figure 2; outcrop 16422F, Figure 5). They are characterized by felsic, garnet-bearing veins of quartzo-feldspatic composition within a metapelitic host rock (Figure 5). The contact between leuco-and melanosome is in parts sharp and resembles an intrusive character (Figures 4g and 4h). The leucocratic domains are characterized by relics of biotite and large white mica of up to 2 mm grain size. A pervasive E-dipping foliation affects both melano- and leucocratic parts (Figure 3d). Leucosomes form asymmetric boudins within an E-dipping foliation (Figure 5b) with N-plunging stretching lineations, associated with N-directed transport (Figure 3d), also shown by other structural indicators such as C′-fabrics (Figures 4j, 4k, 5e, and 5f). A photogrammetric 3D model of the outcrop is hosted on Sketchfab at https://skfb.ly/6TUXJ.

4.2.2. Metamorphic Rocks

Metamorphic rocks at Cer MCC are the result of a contact metamorphic overprint associated with the intrusion of the I-type Qz-monzodiorite. Characteristic index minerals are marked in Figure 2. Outcrop conditions prohibited the mapping of contact relationships between different metamorphic rocks. Thus, they are summarized as "metamorphosed pre-Devonian rocks" in Figure 2. Andalusite-bearing spotted mica schists crop out at the western margin of the intrusion. These fine-grained metapelites host euhedral andalusite-blasts of a few mm diameter, which have overgrown the foliation and were subsequently rotated and almost completely replaced by sericite (Figure 4l). Mylonitic garnet- and staurolite-bearing micaschists (Figures 4a–4f) crop out in the northern part of the Stražanica synform (outcrop 17801J) and at the south-eastern margin of the pluton near Tekeriš (outcrop 17917A). Simultaneous mineral growth and rotation of metamorphic garnet and staurolite led to the formation of snowball structures. Stair-stepping of the tails of these blasts and C′-type shear bands indicate top-NE directed transport. Pyroxene-bearing hornblende mylonites were discovered at the western margin of the main intrusion. They are characterized by a mylonitic foliation composed of quartz and feldspar. Quartz shows dynamic recrystallization by GBM recrystallization and forms elongated ribbons. Feldspar shows grain size reduction and larger relics of plagioclase crystals are only poorly preserved. Diopside formed at the expense of amphibole (actinolite/tremolite) blasts which are clearly in disequilibrium as indicated by the relictic preservation of grains. Relics of garnet are also present (Figure 4g). Accessories include titanite and epidote.

4.3. Thermobarometry

Utilizing the thermobarometer by Ridolfi and Renzulli (2012), results constrain the pressure under which calcic amphiboles crystallized (samples 150906D and 18928D) to ~2 kbar (Figure 7, for results and major-element concentrations, see Table S2). This pressure corresponds to an emplacement depth within the continental crust of the I-type intrusion of 7.5–8 km. Associated crystallization temperatures range between ~720°C and 820°C.

Figure 4. Thin section photomicrographs of igneous and metamorphic rocks from Cer MCC under plane- and cross-polarized light (for locations of the corresponding outcrops see Figure 2). (a) Garnet-bearing mica schist developing C′-type shear bands that indicate top-N transport; (b) garnet-staurolite-bearing micaschist from the south-eastern part of Cer (Tekeriš); (c) Detailed view of Grt from (b) exhibiting snowball structure that indicates syntectonic growth; (d) mylonitic garnet- and staurolite-bearing micaschist from the northern Stražanica-synform, extensional shear bands that developed in s_2 indicate top-N transport; (e and f) y-z- section of the same sample reveals a folded s_1-foliation, resulting in the axial-planar s_2-foliation; (g) garnet- and pyroxene-bearing hornblende-hornfels with mylonitic s_2 foliation (Stražanica-synform); (h) monzodiorite with metamorphic foliation composed of biotite that developed C′-type shear bands, indicating top-N transport; (i) deformed garnet-bearing S-type granite. Prekinematic white mica forming mica fish and S-C-fabric indicate top-N sense of shear; (j) transition between melano- and leucosome of injected migmatites. The leucosome in the lower part is much coarser grained and shows dynamic recrystallization of quartz (subgrain rotation recrystallization). The melanosome is rich in biotite with only minor white mica; (k) Detailed view of the melanosome in (j) with a continuous foliation developing C′-type shear bands that indicate top-N transport; (l) Rotated andalusite-blast, partly replaced by sericite with recrystallized Qz in the strain shadows; (m) Mylonite forming ribbon-quartz, south-eastern part of Cer (Tekeriš); (n) Undeformed Hbl-bearing I-type granitoid; o) Undeformed S-type granite with magmatic garnet.

Tectonics

10.1029/2021TC006699

Table 1
Petrography of Analyzed Samples

Sample	Pos.	Rock type	Mineral assemblage	Structures	Comment	Figures	Long. (°E)	Lat. (°N)
150906D	*FW*	I-type Qz-monzodiorite	Qz + Pl + Kfs + Bt + Hbl ± Ttn ± Ilm	Undeformed	Used for thermobarometry (Section 4.3)		19.511972°	44.595022°
16416B	*SZ*	S-type gneiss	Qz + Pl + Kfs + Wm + Grt ± Trm	SGR/GBM (Qz), C′-type shear bands, mica fish, Top-N		4i	19.533785°	44.581136°
16420D	*SZ*	And-Micaschist	Qz + Pl + Kfs + Wm + And	And forms σ-clasts		4i	19.533785°	44.581136°
16421D	*SZ*	Grt-Micaschist	Qz + Wm ± Bt ± Grt	SGR (Qz), C′-type shear bands, mica fish, Grt forms σ-clasts		4a	19.424847°	44.644850°
16422F1 *18928B*	*SZ*	migmatite; L - leucosome M - melanosome	Qz + Wm + Pl ± Bt ± Grt (L) Qz + Pl + Bt ± Wm ± Grt (M)	SGR (Qz), C′-type shear bands, mica fish	Rocks contain leucocratic and melanocratic domains	4j, 4k, 5	19.470827°	44.645099°
16422F2	*SZ*	–	Only white mica	–	Mica in the neck domain of boudinaged leucosome	5c		
17801I	*SZ*	Pegmatitic dike	Qz + Kfs + Wm ± Grt	SGR (Qz), C′-type shear bands, mica fish		6	19.395085°	44.638187°
17801J	*SZ*	Grt-Micaschist	Qz + Pl + Kfs + Wm + Bt ± Grt ± St	C′-type shear bands, mica fish, σ-clasts	Relic s_1	4e and 4f	19.395085°	44.638187°
17803D	*SZ*	I-type gneiss	Qz + Pl + Kfs + Bt + Hbl + Ttn + Ilm	C′-type shear bands, σ-clasts		4h	19.526935°	44.581674°
17917A	*SZ*	Grt-St-Micaschist	Qz + Kfs/Pl + Wm + Bt ± Grt ± St			4b and 4c	19.531798°	44.564241°
17918D	*SZ*	Hornfels	Qz ± Hbl ± Cpx ± Grt			4g	19.384689°	44.615543°
17918E	*SZ*	S-type gneiss	Qz + Pl + Kfs + Wm + Bt ± Grt	SGR/GBM (Qz), C'-type shear bands, mica fish, Top-N transport lineations			19.392790°	44.616825°
18926C2	*FW*	I-type Qz-monzodiorite (mafic enclave)	Hbl + Bt + Qz + Pl	Undeformed	Mafic enclave		19.463284°	44.637998°
18925H	*FW*	S-type granite	Qz + Kfs + Wm ± Grt	Undeformed			19.392790°	44.616825°
18928D	FW	I-type Qz-monzodiorite	Qz + Pl + Kfs + Bt + Hbl ± Ttn ± Ilm	Undeformed	Used for thermobarometry (Section 4.3)		19.463284°	44.637998°

Note. For locations see Figure 2.

Abbreviations: And, andalusite; Bt, biotite; Grt, garnet; GBM, grain boundary migration recrystallization; FW, footwall; Ilm, ilmenite; Kfs, potassium feldspar; Pl, plagioclase; Qz, quartz; St, staurolite; SGR, subgrain rotation recrystallization; SZ, shear zone; Ttn, titanite; Wm, white mica.

4.4. Results of $^{40}Ar/^{39}Ar$ Geochronology

Ar-isotope compositions of potassium-bearing minerals from seven samples were analyzed by multi-grain step heating, in situ, single-grain total fusion, and single-grain step heating techniques. We sampled undeformed I- and S-type igneous rocks from the undeformed footwall as well as deformed rocks from the shear zone (sample locations are marked in Figure 2, for mineral parageneses and sample petrography see Table 1; dating methods and results are summarized in Table 2; for complete data sets see supplementary files DS01-DS04 at https://zenodo.org/record/4678734).

4.4.1. $^{40}Ar/^{39}Ar$ In Situ Geochronology

Five sample discs were prepared from sample 16422F1 (Figure 5d) for $^{40}Ar/^{39}Ar$ in situ analyses. The validity of the analyses was tested by analyzing the standard HD-B1 by in situ laser ablation. This yielded ages identical within uncertainty to the age reported by Schwarz and Trieloff (2007), which was recalculated to the same decay constant and fluence monitor as for our calculations (Section 3.2). All together 124 spots targeting white mica and 13 spots on biotite were analyzed (Table S1, Figure 8, DS01). At very low signal intensities on mass 40, a systematic correlation between the degree of blank correction and age was observed, which is why measurements that yielded a blank/signal ratio above 1:5 ($n = 49$) were discarded. Of the remaining data set, 12 analyses yielded ^{36}Ar signals below the CDD detection limit ($\sim 5 \times 10^{-20}$ mol ^{36}Ar), meaning that an atmospheric correction for these spots was not possible. A comparison with analyses where signal intensities for ^{36}Ar were measurable and thus atmospheric correction was possible, reveals a significant difference in ages, as exemplarily shown for analyses of WM from the leucosome with WMA of 17.89 ± 0.08 Ma for the uncorrected data and 17.32 ± 0.12 Ma for the data including atmospheric correction (Figure 8a). In addition, the associated age uncertainties for spots without atmospheric correction are underestimated due to the missing propagation of the uncertainty of the ^{36}Ar measurement (Figures 8a and 9i). Therefore, only measurements with ^{36}Ar above the detection limit are considered for further evaluation. Individual spots yield ages that range from 16.25 ± 0.99 to 18.14 ± 0.84 Ma for white mica. Ages for both leuco- and melanosome are identical within uncertainty (Figure 8). The inverse isochron age for 56 white mica spots from the leucosome is 17.30 ± 0.17 Ma with an initial $^{40}Ar/^{36}Ar$ ratio of 300.2 ± 8.4 (MSWD = 0.32; Figure 8b), identical to the inverse isochron age for white mica from the melanosome of 17.05 ± 0.43 Ma ($n = 7$, Figure 8d). Intra-granular age variations were not observed and the inverse isochron ages of analyses obtained on individual grains scatter around 17.3 Ma with initial $^{40}Ar/^{36}Ar$ ratios almost identical to the atmospheric Ar composition (Figure 9, inset Figure 11b).

4.4.2. $^{40}Ar/^{39}Ar$ Step Heating

Five mineral separates from samples 16422F2, 18925H, and 18926C2 were dated using the step-heating technique (Table 2, Figure 10, Table S1, DS04). Experiments consisted of 16–18 heating steps with 86%–99% of ^{39}Ar released. WPAs were calculated using the initial $^{40}Ar/^{36}Ar$-ratio yielded by the corresponding isochron plot, where it significantly deviated from the atmospheric $^{40}Ar/^{36}Ar$-composition of 298.6 ± 0.3.

4.4.3. $^{40}Ar/^{39}Ar$ Single-Grain Total Fusion- and Step Heating Experiments

Single-grain total fusion (SGTF) and step heating (SGSH) experiments were carried out on three deformed samples of the shear zone (samples 17918E, 17801I, and 18928B; grainsize fractions 80–250 μm, 250–500 μm, 500–1,000 μm, and 1–2 mm). Results are summarized in Figure 12 and Table 2. Complete data sets and additional isochron plots and age spectra for both, SGTF and SGSH analyses can be found in the electronic supplement to this article (DS02, DS03, Figures S1 and S2). The WMA of the respective grain size fractions for each sample were calculated using a modified Chauvenet Criterion to detect and reject outliers (for further details see Vermeesch, 2018).

SGTF analyses yielded WMAs ranging between 17 and 18 Ma. For sample 18928B white mica from the leucosome and biotite from the melanosome were analyzed yielding identical ages. MSWD values for all analyzed fractions range between 0.5 and 2.0 with one exception of sample 18928B (leucosome), fraction 250–500 μm (MSWD = 0.25). SGTF ages of sample 17918E show the largest age scatter of grainsize 80–250 μm, ranging between 13.6 ± 2.4 and 21.5 ± 1.4 Ma with an outlier at 31.3 ± 6.2 Ma that is not overlapping with the corresponding WMA within uncertainty.

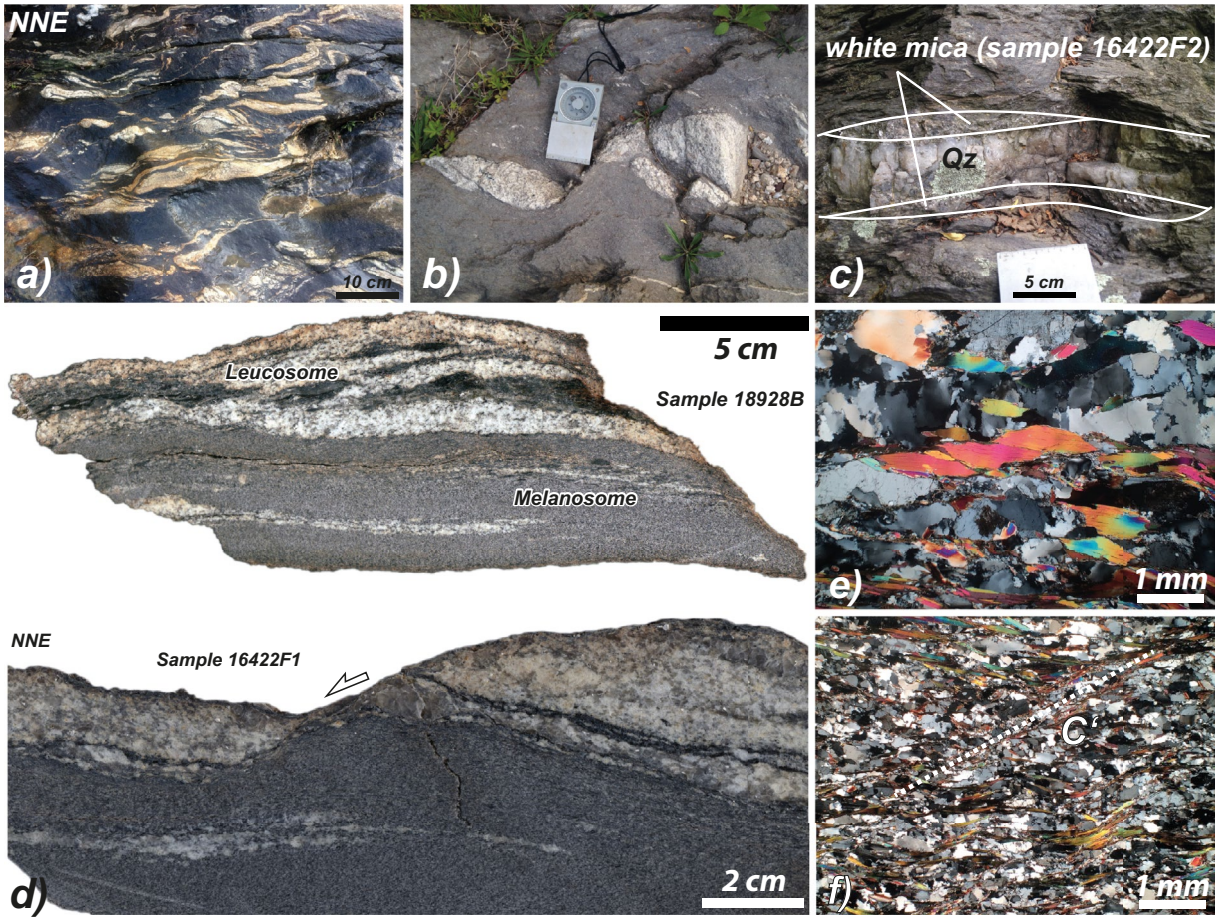

Figure 5. (a and b) Outcrop 16422F near Bela Reka exposing injected migmatites, i.e., injected leucosomes in a melanocratic host rock. (c) Quartz mobilisations associated with the accumulation of white mica (Sample 16422F2 – used for step-heating dating). (d) Detailed view of samples 16422F1 and 18928B. Asymmetric boudins and the nebulous occurrence of leucocratic material in the lower left. (e and f) Thin section micrographs of the leucosome and melanosome of the rock. Note that only relics of biotite are present in the leucosome. Both domains show mica fish and C′-type shear bands.

Single-grain step heating (SGSH) analyses were obtained from grain-size fractions 1–2 mm (17918E) and 0.5–1 mm (17801I and 18928B). Most step-heating analyses of single grains consisted of 5–9 heating steps resulting in well-defined plateau sections of consecutive steps comprising 55%–100% of ^{39}Ar released. Four out of five grains from sample 17801I show age spectra that display slightly older ages within the first respective heating steps. Initial ^{40}Ar/^{36}Ar ratios between 306.9 ± 2.8 and 312.9 ± 1.4 are slightly elevated with respect to the atmospheric ^{40}Ar/^{36}Ar composition. Inverse isochron ages were calculated for both SGTF- and SGSH analyses. For a comparison of the results, initial ^{40}Ar/^{36}Ar-ratios were plotted against the inverse isochron ages (Figure 11b). The SGTF inverse isochron ages show a larger scatter and display larger uncertainties associated with the initial ^{40}Ar/^{36}Ar-ratio but are mostly identical to the SGSH inverse isochron ages within uncertainties. SGSH analyses of sample 17801I show the highest initial ^{40}Ar/^{36}Ar-ratios of up to 312.9 ± 1.4, followed by sample 17918E with values up to 302.1 ± 6.2. SGSH analyses of sample 18928B show initial ^{40}Ar/^{36}Ar-ratios of atmospheric composition and also the youngest inverse isochron ages of 17.01 ± 0.07 to 17.21 ± 0.12 Ma for Bt and 17.16 ± 0.05 Ma for white mica.

4.5. Cross Section

We constructed a balanced NNE-striking cross-section, 100 km in length, across the most internal Dinaridic nappe contact between the Jadar-Kopaonik- and the Drina-Ivanjica nappes using the Move Suite (Petroleum Experts Ltd.; e.g., Egan et al., 1997). For simplicity, the obduction of the western Vardar ophiolites

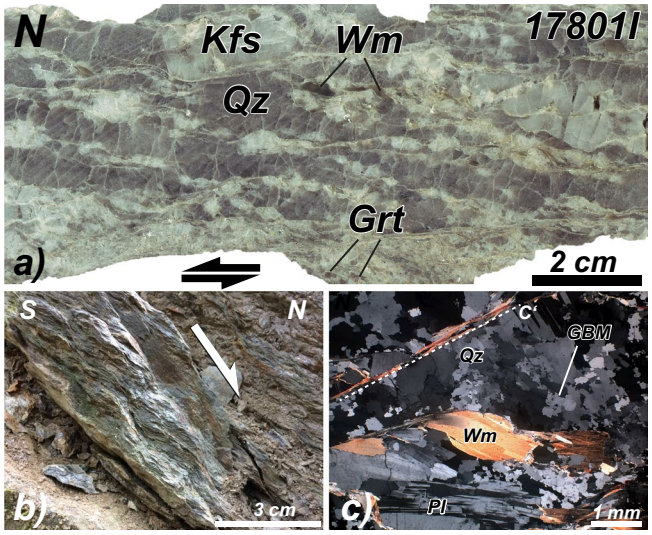

Figure 6. Detailed view of a deformed pegmatitic dike that intruded into the shear zone (for location see Figure 2). (a) Overview of sample 17801I. Compositional layering of Qz and Kfs forms the foliation. (b) Wall rock composed of amphibolite-grade metapelites developed C′-type shear bands. (c) Deformed white mica fish and C′-fabric indicate the top-N sense of shear. Qz shows dynamic recrystallization by grain boundary migration (GBM). Pl shows deformation twinning.

in Late Jurassic times (Robertson et al., 2009) is not shown. The nappe contact between the Drina-Ivanjica- and the East-Bosnian-Durmitor thrust sheets is characterized by a long flat segment, followed by a ramp segment in the area of the Drina river (Figure 12). A similar geometry has been proposed by Nirta et al. (2020). Forward modeling of this Cretaceous-Paleogene shortening results in a minimum displacement of the Drina-Ivanjica thrust sheet of 70 km with SW-directed transport.

The breakaway fault of the extensional Cer detachment roots in the extensionally reactivated ramp segment of the nappe contact between the Jadar-Kopaonik- and Drina-Ivanjica thrust sheets and juxtaposes Early Triassic rocks in the hanging wall against Paleozoic strata in the footwall (Figure 12). Two additional listric fault segments of the detachment system are located further north, of which the first juxtaposes Late Cretaceous carbonates against Early Triassic units. The second fault bounds Miocene sediments south of Cer against Late Cretaceous carbonates. The detachment reaches a depth of ~7.5–8 km, based on estimations of the crystallization depth of the I-type Qz-monzodiorite (Figure 7, Section 4.3). The flat segment of the extensional shear zone is presumably located within pre-Devonian strata. It exhumed the plutonic rocks together with their greenschist-to lower amphibolite facies envelope of Devonian to Carboniferous age. A kinematic forward model was constructed to determine the displacement along brittle structures during extension. Using the simple shear algorithm, the displacement along the breakaway fault and the two listric fault segments further north amounts to a total of 3.5 km, with a total horizontal offset of ~2 km. Simple line-length balancing yields an additional 12 km of horizontal offset for the ductile shear zone (Figure 13).

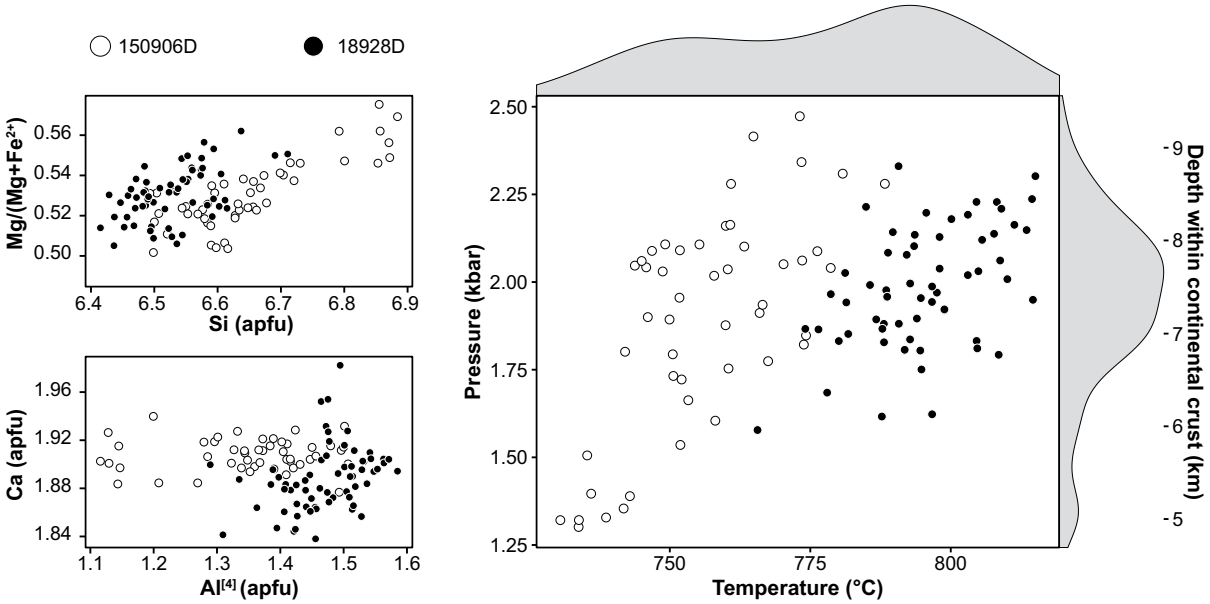

Figure 7. Mineral chemistry of calcic amphiboles of two samples from the I-type granitoid used for thermobarometry after Ridolfi and Renzulli (2012). Left: XMg versus Si and Ca versus $Al^{[4]}$ diagrams. Right: Results of thermobarometric calculations of the same samples. A broad maximum exists at ~2 kbar, constraining the crystallization depth to 7.5–8 km.

Tectonics

10.1029/2021TC006699

Table 2
Age-Results of Ar-Ar Geochronology Obtained by Different Techniques

Sample	Position	Rock type		Mineral	Technique		grain size/ spot size (μm)	WPA/ WMA (Ma)	±1σ	MSWD	IIA (Ma)	±1σ	MSWD	No of aliquots used WMA/IIA/Tot	$(^{40}Ar/^{36}Ar)_i$	±1σ
16422F1	SZ	migmatite	L	Wm	IS	All	200–250	17.32	0.06	0.3	17.30	0.08	0.32	56/56/56	300.2	4.2
						SG	250	17.30	0.31	0.03	17.11	0.93	0.02	4/4/4	319	97
							250	17.28	0.26	0.19	17.12	0.38	0.14	6/6/6	315	27
							250	17.38	0.18	0.37	17.36	0.26	0.46	6/6/6	299.3	9.6
							250	17.29	0.12	0.56	17.29	0.17	0.77	5/5/5	298	17
			M			All	200–250	17.39	0.31	2.3	17.05	0.17	0.46	7/7/7	313.9	4.5
						SG	200–250	16.96	0.19	0.01	16.94	0.54	0.02	4/4/4	304	186
18928B	SZ		L	Wm	SGTF	MSG	80–250	17.23	0.14	0.83	17.19	0.13	0.87	30/30/30	301.2	6.2
							250–500	17.14	0.04	0.25	17.06	0.11	0.2	23/22/23	304.9	7.0
			M	Bt			80–250	17.11	0.12	0.64	16.93	0.16	0.59	34/32/34	300.6	1.4
							250–500	17.03	0.06	1.4	17.08	0.09	1.2	32/31/33	298.04	0.75
			L	Wm	SGSH	SG	500–1000	17.17	0.05	5.3	17.16	0.05	3.6	22/31/31	301.16	0.59
			M	Bt				17.01	0.09	0.97	17.06	0.11	1.1	5/5/5	297.2	2.0
								17.02	0.07	0.88	17.01	0.07	1.1	5/5/5	299.01	0.75
								17.19	0.10	0.91	17.19	0.09	1.2	5/5/5	298.69	0.95
								17.08	0.09	0.62	17.01	0.10	0.62	5/5/5	297.8	1.0
								17.09	0.08	0.86	17.10	0.08	1.1	4/4/4	298.01	0.97
								17.14	0.12	0.15	17.21	0.12	7.4	3/4/4	300.0	1.3
17801I	SZ	pegmatite		Wm	SGTF	MSG	80–250	17.88	0.09	0.59	17.67	0.14	0.45	30/30/32	304.4	2.6
							250–500	17.41	0.02	2.0	17.32	0.06	2.3	33/33/33	302.72	0.78
					SGSH	SG	500–1000	17.26	0.05	3.0	17.22	0.05	1.7	7/7/9	306.9	2.8
								17.27	0.05	10.5	17.26	0.05	11	5/6/8	307.9	1.2
								17.31	0.05	0.17	17.29	0.05	0.2	3/4/4	311.0	1.7
								17.46	0.05	43	17.45	0.05	37	4/6/6	312.9	1.4
								17.45	0.05	15	17.46	0.05	21	3/6/6	308.6	1.4
17918E	SZ	S-type gneiss		Wm	SGTF	MSG	80–250	18.00	0.16	0.97	17.96	0.24	0.81	30/30/28	301.5	8.6
							250–500	17.78	0.11	0.87	17.70	0.18	0.38	29/23/30	298.3	2.3
							500–1,000	17.44	0.04	0.55	17.35	0.09	0.56	33/33/34	301.3	1.6
					SGSH	SG	500–1,000	17.31	0.06	7.21	17.28	0.05	7.1	4/4/5	301.7	1.1
								17.46	0.06	2.6	17.41	0.05	3.3	6/5/6	302.1	6.2
								17.35	0.05	1.13	17.31	0.07	1.4	3/3/8	301.6	3.2
								17.27	0.36	1.24	17.36	0.05	1.4	6/6/6	298.13	0.63
								17.33	0.05	0.78	17.33	0.05	0.91	6/6/6	299.1	1.1
16422F2	SZ			Wm	SH	MG	500–1500	16.35	0.18	0.29	16.35	0.28	0.32	15/15/15	350.0	48

Table 2
Continued

Sample	Position	Rock type	Mineral	Technique	grain size/ spot size (μm)	WPA/ WMA (Ma)	±1σ	MSWD	IIA (Ma)	±1σ	MSWD	No of aliquots used WMA/IIA/Tot	$(^{40}Ar/^{36}Ar)$ i	±1σ
16925H	FW	**S-type granite**	Wm	SH	500–1500	16.62	0.10	0.64	16.66	0.11	0.65	14/14/16	290.0	9.0
18926C2	FW	**I-type granite** mafic enclave	Bt	SH	500–1,000	17.32	0.15	0.24	17.44	0.14	1.6	13/18/18	294.8	0.21
			Hbl		250–500	16.8	1.0	0.44	16.7	1.2	0.73	4/4/18	315.6	2.4
						25.01	0.38	2.86	25.40	0.55	3.3	13/13/18	324	14

Abbreviations: Bt, biotite; FW, footwall; Hbl, hornblende; IIA, inverse isochron age; IS, in situ Laser-ablation; L, leucosome; M, melanosome; MG, multi-grains (mineral separate); MSG, multiple single grains; MSWD, mean square of weighted deviates; SH, step heating; SGSH, single grain step heating; SGTF, single grain total fusion; SZ, shear zone; Tot, total number of aliquots; SG, single grain; WPA, weighted plateau age; Wm, white mica; WMA, weighted mean age.

5. Discussion and Interpretation

The concept of MCCs was originally developed for the Basin and Range Province in the North American Cordillera (e.g., Davis & Coney, 1979; Lister & Davis, 1989; Wernicke, 1985) and later applied to other regions, for instance, the core complexes in the Cycladic archipelago, located in the Aegean Sea (Lister et al., 1984). Cordilleran-type core complexes are characterized by several distinct structural features. These include (a) a mylonite zone below a low-angle detachment, which separates the metamorphic carapace surrounding the metamorphic core from unmetamorphosed strata, (b) homogenously oriented stretching lineations exclusively associated with identical transport directions, and (c) an overall extensional regime (e.g., Davis et al., 1980; Davis & Coney, 1979; Platt et al., 2015). Although the Cer massif might not be viewed as a MCC in the strictest sense, it shows striking similarities to Cycladic MCCs, where a close interconnection between magmatic activity and detachment faulting, as well as the reactivation of inherited thrust contacts, plays an important role during exhumation (Jolivet et al., 2010; Rabillard et al., 2018).

Cer MCC is one of the few places in the internal Dinarides that exposes such structures, including a ductile low-angle extensional shear zone associated exclusively with top-N transport and active in the early Miocene. Other locations characterized by a similar structural evolution include the Motajica and Prosara core complexes in the northwest (Ustaszewski et al., 2010), Fruška Gora (Toljić et al., 2013) to the north, and Kopaonik-Studenica (Schefer et al., 2011) in the south (Figure 2), where a significant amount of extension was accommodated by top-N transport.

5.1. Methodical Considerations

The age determination of different generations of minerals in a sample with a complex structural history by means of $^{40}Ar/^{39}Ar$ geochronology is a challenging task and as bulk sample fusion methods may lead to mixed-age signals containing several mineral growth generations, the focus has shifted toward single-crystal dating (e.g., Uunk et al., 2018; Wijbrans et al., 1990) and in situ UV-laser-probe dating (e.g., Kelley, 2002; Schneider et al., 2013). $^{40}Ar/^{39}Ar$ in situ geochronology provides a powerful tool when it comes to the determination of inter- and intra-granular age variations of potassium-bearing minerals while maintaining structural control of a sample. The amount of radiogenic Ar liberated by an ablation spot depends on the ablation volume, age, and K-content of the mineral of interest and is much smaller compared to single- or multi-grain step heating techniques, which make use of the whole grain(s), thus resulting in lower signal intensities and therefore larger uncertainties. In addition, the potential lack of atmospheric correction due to undetectable ^{36}Ar complicates the interpretation of ages. Therefore, we additionally separated individual grains and dated several grain-size fractions by the multiple single-grain total fusion (SGTF). Nevertheless, SGTF measurements lack the ability to gather information about intra-granular age information that may indicate growth or diffusion as well as information about the local kinematic background (pre- or synkinematic) of a grain. However, in contrast to multi-grain step heating, multiple SGTF is able to resolve different age populations in a sample if it is assumed that argon loss and contributions from excess argon can be neglected. For some samples, we therefore applied single grain step heating (e.g., Wijbrans et al., 1990) that combines the advantages of the multi-grain step heating technique, i.e., detection of argon loss and excess argon, with the ability to resolve different mineral age generations within a sample.

Our approach combining multi-grain step heating, multiple single grain total fusion/step heating, and in situ ablation on different grain size fractions of deformed samples from the shear zone enables us to resolve a maximum of information and to cross-check the individual results on their internal consistency.

5.1.1. Closure Concept and Diffusion

The closure temperature concept (Dodson, 1973) states that when a mineral cools below a specific temperature (closure temperature T_c), the diffusion rates in minerals of interest become insignificant even in geological time scales, meaning in the case of argon isotopes the system

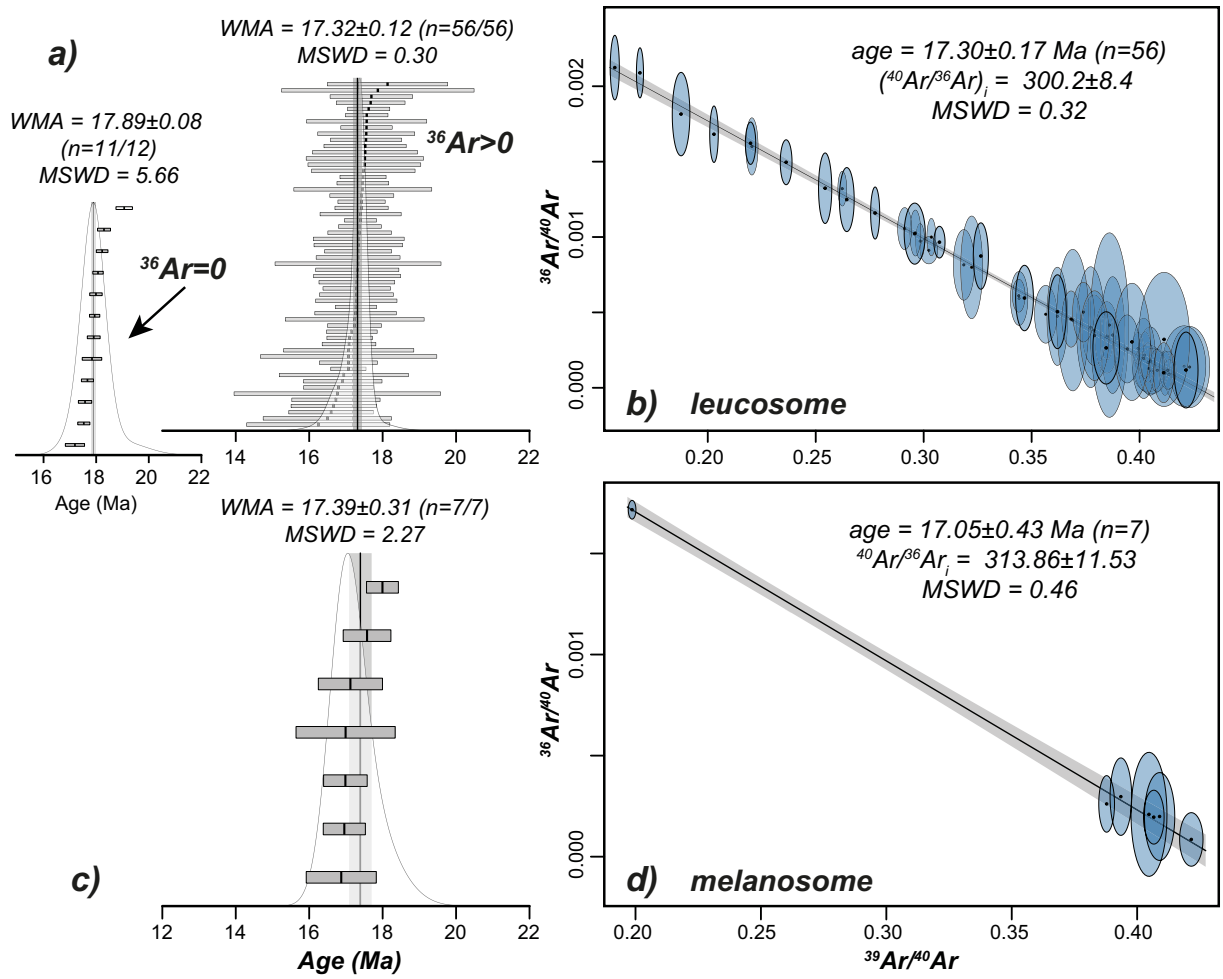

Figure 8. Rank order plots with weighted mean ages (WMA) and inverse isochron plots of white mica (sample 16422F1) obtained by in situ laser ablation dating. Analytical uncertainties are shown on a 95% confidence level. MSWD, mean square of weighted deviates. (a) Data with and without atmospheric correction due to ^{36}Ar signals below the detection limit. The lack of atmospheric correction leads to a weighted mean age that is significantly older than the WMA of aliquots corrected for atmospheric Ar. (b) Inverse isochron plot of the same spot analyses as shown in (a) of the leucosome. (c and d) WMA and IIA plot of white mica of the melanosome.

is "closed" and neither gains (i.e., excess Ar) nor loses ^{40}Ar, and hence all radiogenic Ar is retained in the crystal. When a mineral has not yet cooled below T_c, radiogenic ^{40}Ar is either merely retained partially or, at higher temperatures, completely lost, leading to a resetting of the Ar-isotopic system (Dodson, 1973). The closure temperature depends on the cooling rate of a mineral and the effective grain size. For instance, a muscovite grain with a radius of 100 μm cooling at a rate of 10°C/Ma at 5 kbar has a corresponding closure temperature of 405°C (Harrison et al., 2009). For Biotite, a closure temperature of 290°C–320°C is reported (Grove & Harrison, 1996; Schaen et al., 2020), depending also on the geochemical composition. Hornblende of equal dimensions cooling at a rate of 10°C/Ma has a closure temperature of 510°C (Harrison, 1982). The dominant process governing the mobility of Ar is by volume diffusion, which strongly depends on the temperature, although crystal defects, as well as subgrain boundaries, can serve as fast-diffusion pathways (Lee, 1995). Diffusion can either lead to Ar loss, i.e., migration of ^{40}Ar out of the grain, for example through percolating intra-granular fluids, or to excess argon (Kelley, 2002) that can originate from older K-bearing minerals and is subsequently incorporated in the mineral of interest (Kuiper, 2002). Other processes that lead to the complete reset of the Ar-isotopic system are fluid-assisted processes and recrystallization.

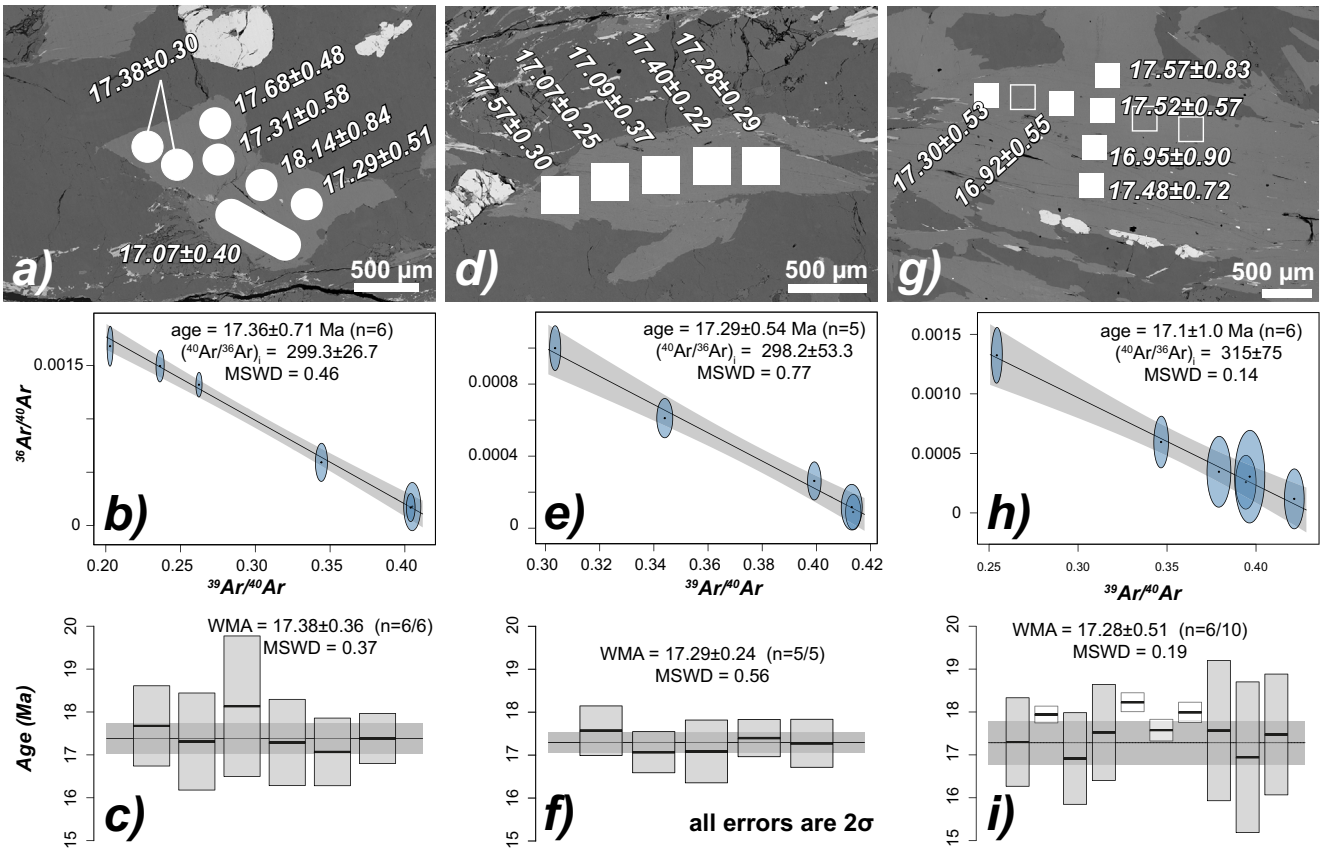

Figure 9. Examples of intra-granular dating of white mica from the low-angle shear zone (sample 16422F1) with BSE images showing spot sites (top row; filled: with atmospheric correction, empty: no atmospheric correction due to ^{36}Ar signal below detection limit) and inverse isochron plots and weighted mean ages (middle and bottom row, respectively). Note that the ages without atmospheric correction (white bars in (i)) are slightly older (too much ^{40}Ar) and have lower uncertainties (no propagation of the uncertainty of the ^{36}Ar signal into the final age).

5.1.2. Validity of the Data

In order to cross-check the results of the individual dating methods on their internal consistency, in situ, SGTF and SGSH analyses obtained on samples 16422F1 and 18928B (Figure 5d), which come from the same outcrop, were compared. In general, all methods yield ages identical within uncertainty. Furthermore, in situ analyses revealed no systematic intra-granular age variations, indicating that Ar-mobility by diffusion and the role of excess Ar are minor. The same holds for SGSH analyses. White mica and biotite show no signs of excess argon or Ar loss, indicated by undisturbed age spectra (Figure S2). Inverse isochron ages of biotite range between 17.01 ± 0.21 and 17.21 ± 0.52 Ma with an initial ^{40}Ar/^{36}Ar ratio between 297.2 ± 6.5 and 300.0 ± 5.5. WM yields an inverse isochron age of 17.16 ± 0.10 with an initial ^{40}Ar/^{36}Ar ratio of 301.2 ± 1.2 (Figures 11b and S1). These ages are identical to those obtained by the in-situ technique. SGTF analyses of sample 18928B yield grain size dependent WMAs of 17.23 ± 0.14 and 17.14 ± 0.04 Ma for white mica and 17.11 ± 0.24 Ma and 17.03 ± 0.12 Ma for biotite (Figure 11). The age distribution is unimodal, which indicates that Ar-mobility affected all grains equally and only one generation of mica growth is present.

5.2. Evolution of the Cer Massif

A conceptual model combining our field observations with geochronological results is shown in Figure 13. The concept involves a simple, balanced forward model that accounts for Late Cretaceous shortening and Oligo-Miocene extension (Figure 13). Time step 1 depicts the evolution of the Adriatic margin during Late Cretaceous nappe-stacking: the Jadar-Kopaonik composite nappe is thrust onto the Drina-Ivanjica nappe, followed by the in-sequence emplacement onto the East Bosnian-Durmitor thrust sheet (e.g., Schmid

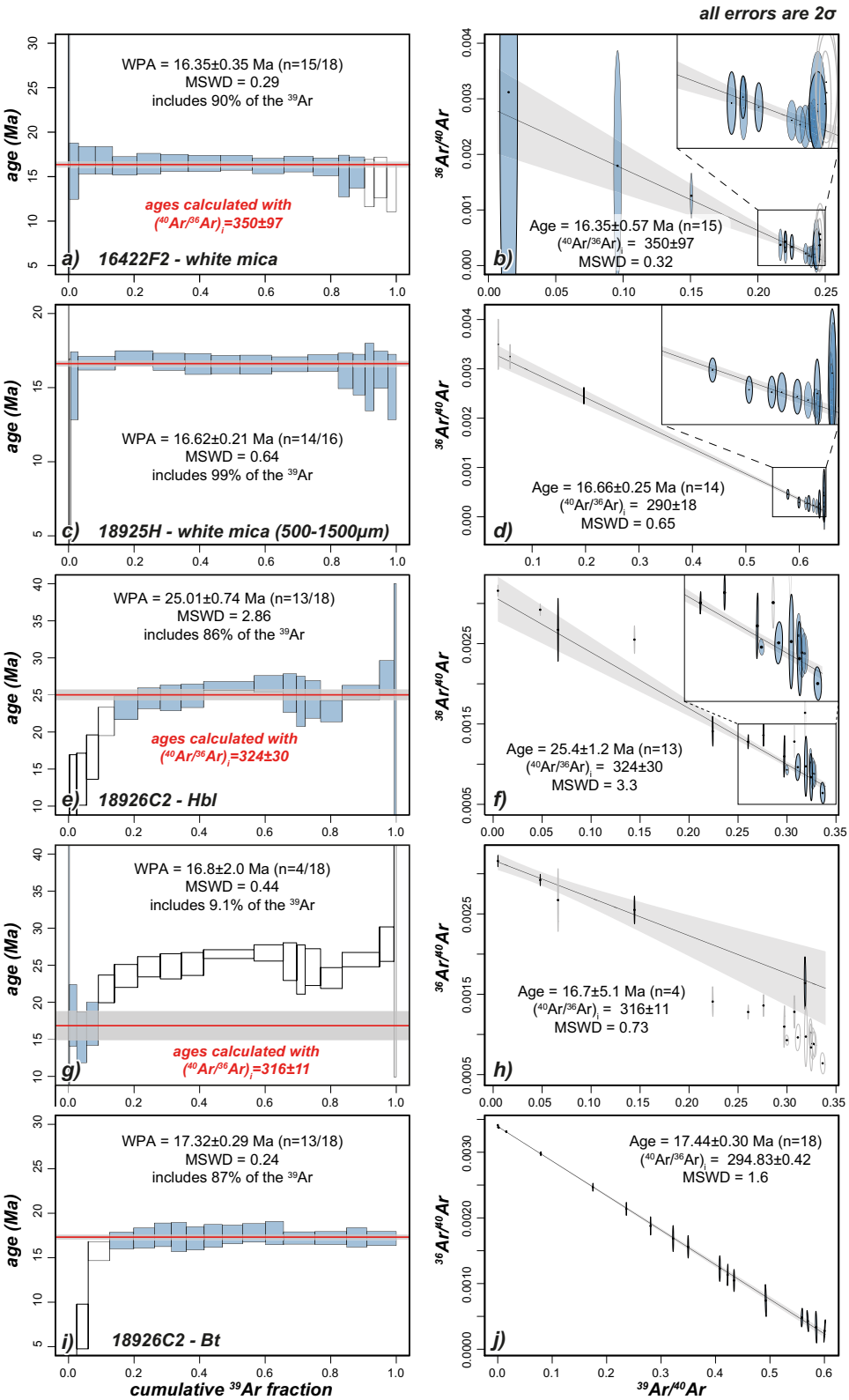

Figure 10. Age spectra and inverse isochron plots of step-heating experiments. (a and b) White mica from a boudined leucosome of the low-angle shear zone (16422F2 – Figure 4c). (c and d) White mica from an undeformed S-type granite below the shear zone (18925H). (e and f) Amphibole from I-type granitoid (18926C2). (g and h) Recalculation of the age spectrum in (e) with an initial $^{40}Ar/^{36}Ar$-ratio of 316 ± 11, determined by the inverse isochron through the first four steps (h). (i and j) Biotite from the same sample (18926C2). The age spectrum indicates Ar-loss for the low-temperature steps.

et al., 2020), which likely led to the development of the layer-parallel foliation s_1. Step 2 shows the situation after the shortening had migrated into the external Dinarides (not pictured). This was followed by the Oligocene emplacement of the I-type intrusion of Cer, which in turn led to a local rotation of s_1 into a subvertical orientation. The onset of the extension during the early Miocene (step 3) involved the extensional reactivation of the ramp segment of the formerly contractional contact between the Jadar-Kopaonik and the Drina-Ivanjica nappes. Further extension led to the formation of three listric fault segments, which root in an extensional low-angle shear zone at a depth of ~7–8 km (steps 4–5). Continued crustal extension (step 6) induced warping of the exhuming middle crust into a dome (e.g., Wernicke, 1985), associated with the emplacement of S-type melts (e.g., Lister & Baldwin, 1993). Such structures have also been observed in the Pannonian Basin, for example in the Great Hungarian Plain, where the WNW part of the Derecske subbasin exhumes Mesozoic metamorphic rocks (Balázs et al., 2016); as well as in the Pohorje dome at the westernmost margin of the Pannonian Basin (Fodor et al., 2020). The driving forces responsible for the exhumation of Cer are ambiguous but might involve isostatic reequilibration of hot mantle lithosphere due to tectonic denudation (Lister & Davis, 1989; Wernicke, 1985) or lower crustal flow (Block & Royden, 1990).

Thermobarometry on I-type Qz-monzodiorite samples indicates a crystallization depth of 7–8 km, which also constrains the depth of the mylonitic shear zone, given the fact that it affected the top of the I-type intrusion, while the central part appears undeformed. The depth of 7–8 km likely corresponded to ambient temperatures of c. 210°C–240°C in the country rocks, assuming that the regional geotherm was not particularly elevated, as the age of the I-type intrusion predates rifting in the Pannonian Basin by c. 10–12 Ma. As quartz shows recrystallization by subgrain rotation, indicating at least 400°C during deformation (Stipp et al., 2002a), an elevated geothermal gradient of up to 50°C/km must have prevailed during subsequent deformation, facilitating ductile deformation. This local restriction of ductile deformation has also been described for the Tonale fault zone in the Italian Alps (Stipp et al., 2002b) and for instance in the Colorado River extensional corridor (Lister & Baldwin, 1993; Reynolds & Lister, 1990).

Cooling of the I-type intrusion by conductive heat transfer into the surrounding host rocks led to an amphibolite-grade contact metamorphic overprint, resulting in the formation of staurolite, metamorphic garnet, hornblende, and clinopyroxene. The growth and subsequent rotation of andalusite-blasts from the shear zone at the western margin of the pluton (Figures 2 and 4i) indicates ongoing deformation during a later stage of the metamorphic evolution.

At c. 25.4 Ma, the I-type intrusion cooled below ~500°C, as demonstrated by our Hbl-age (Figures 10g and 10h). Biotite of the same sample yields an inverse isochron age of 17.4 ± 0.3 Ma. The intrusion of the S-type granite before 16.6 Ma led to a thermal overprint of parts of the I-type qtz-monzodiorite. This is apparent from the age spectra of Hbl and Bt (18926C2; Figures 10g–10j). The age spectrum of biotite shows signs of Ar-loss with the first 5 steps considerably younger than the WPA, indicating that Ar was mobilized and removed from the outer parts of the mineral grains. The thermal overprint lasted not long enough to completely reset biotite, as indicated by the well-defined plateau (Figure 10i, steps 6–18). The thermal impulse of the S-type intrusion was followed by local cooling, indicated by an Ar-Ar SH white mica age of 16.66 ± 0.25 Ma (IIA Wm, Figure 10d). Cooling ages obtained on white mica from the S-type granite are compatible with published K-Ar ages of white mica ranging between 15.96 ± 0.64 and 16.48 ± 0.65 Ma (Koroneos et al., 2011). Ductile deformation in the shear zone accommodated during top-N transport is indicated by shear sense indicators such as sigma-clasts and C′-type shear bands that developed in both the mylonitic metapelites and the intrusive rocks (I- and S-type). Ages obtained on these rocks are slightly older compared to the undeformed footwall. Ductile deformation accommodated by the extensional shear zone lasted until late Early Miocene, constrained by the youngest Ar-ages obtained on shear zone rocks at c. 17 Ma (Figure 11b). Similar ages for white mica and biotite indicate fast cooling below the respective closure temperatures, facilitated by tectonic exhumation.

A step heating inverse isochron age of 16.35 ± 0.57 Ma obtained on white mica associated with Qz mobilisates (Figure 5c; 16422F2) indicates a longer duration of hydrothermal activity, which also explains the initial $^{40}Ar/^{36}Ar$-ratio of 350 ± 45 (1σ). This deviates significantly from the atmospheric composition due to the incorporation of excess-Ar. A sample with an elevated initial $^{40}Ar/^{36}Ar$-ratio is 17801I (Figures 11b), a pegmatite that intruded the shear zone. SGSH age spectra indicate that Ar trapped in the respective crystals has a component of excess Ar. Pegmatites are usually associated with increased amounts of hydrothermal

fluids that are able to carry extraneous Ar, which is then incorporated into the growing minerals. Contemporaneous deformation created additional intra-granular pathways for the Ar-transporting fluids.

Zircon and apatite fission track data (16.5–16.1 Ma and 14.4 Ma, respectively; Stojadinovic et al., 2017; Ustaszewski et al., 2010) of samples located near or within the shear zone yielded older ages in comparison to samples from the footwall, i.e., the undeformed portion of the intrusion (15.1 Ma for Zr and 12.5 Ma for Ap; Figure 14a).

5.3. Regional Implications

N-S-extension of Early Miocene age led to extensional reactivation of the ramp segment of the Cretaceous nappe contact separating the Jadar-Kopaonik and Drina-Ivanjica thrust sheets (Figures 12 and 13). This segment forms the structurally deeper part of the break away fault of the detachment. The Drina-Ivanjica thrust sheet only shows minor folding of Paleozoic strata, which can be attributed to earlier shortening during Late Cretaceous SW-vergent nappe-stacking. Restoration of the nappe structure by stepwise removal of extensional deformation yields a nearly perfect flat-ramp-flat geometry (Figures 12 and 13).

An equivalent to the Cer MCC can be found in the Kopaonik-Studenica region (Figure 1), where rocks comprising Paleozoic to Mesozoic metapelites up to amphibolite-grade of the Jadar-Kopaonik composite nappe (Schefer et al., 2010) were exhumed in Early Miocene times, along with Oligocene (31.77–30.70 Ma) I-type and Miocene (20.6–17.7 Ma) S-type granitoids (Schefer et al., 2011). Here, the emplacement of the S-type granite during N-S-directed extension preceded a phase of rapid cooling between 16 and 10 Ma due to exhumation of the core complex (Schefer et al., 2011).

Miocene extension has also been observed in more external parts of the Dinarides, for instance in the Ibar- and Sarajevo-Zenica basins in the vicinity of Sarajevo in Bosnia and Hercegovina (Andrić et al., 2015, 2017) and in the southern external Dinarides (Van Unen et al., 2019). Records of extension in the Sarajevo-Zenica region are restricted to the basin, where the deposition of syn-rift sediments started in the Lower to Middle Miocene, associated with syn-depositional normal faulting during NE-SW extension (Andrić et al., 2017). Ages derived from magneto-biostratigraphy date the onset of extension-related sedimentation to 17.2 Ma (Sant et al., 2018). In a more internal position, within the Sava suture zone, the onset of the extension was dated to 25 to 21 Ma (Ustaszewski et al., 2010). The process triggering Oligo-Miocene extensional deformation in the internal Dinarides is still under debate. Schefer et al. (2011) proposed a model involving the removal of mantle lithosphere by mantle delamination to account for a “slab gap” underneath the external Dinarides (Handy et al., 2015; Subašić et al., 2017) and to explain the emplacement of Oligocene magmatic, partly ultrapotassic rocks with mantle affinity (Cvetković et al., 2007; Prelević et al., 2005). Evidence in favor of this model was provided by Casale et al. (2013), who showed that the Mid-Bosnian Schist Mountains, located further externally with respect to Cer, also represent a MCC that was exhumed between 43 and 27.5 Ma, with rapid cooling occurring between 35 and 27 Ma—coincident with the timing of slab-breakoff and subsequent mantle delamination proposed by Pamić et al. (2002) and Schefer et al. (2011). This hypothesis is further supported by evidence for regional uplift during Oligocene times (Balling et al., 2021).

Considering these geochronological and kinematic observations, we conclude that there were differing processes triggering the exhumation of MCCs across the Dinaric orogen. Exhumation of Oligocene core complexes, such as the Mid-Bosnian Schist Mountains (Casale et al., 2013) was rather triggered by delamination of the Adriatic mantle lithosphere beneath the external part during early Oligocene times. This delamination presumably led to the formation of melts originating from the lower crust and the emplacement of such rocks of I-type composition in the middle crust (Schefer et al., 2011). The exhumation of early Miocene core complexes in the internal part of the Dinarides, however, was the result of the roll-back of the European slab beneath the Carpathians. The latter process is overall responsible for the opening of the Pannonian Basin. This view is supported by the fact that the overall amount of extension seems to decrease toward the external Dinarides, where it is restricted to early Miocene sedimentary basins, while in the internal Dinarides much larger amounts of the extension were recorded by the exhumation of mid-crustal core complexes. Furthermore, the proposed rollback of the Adriatic slab, previously suggested

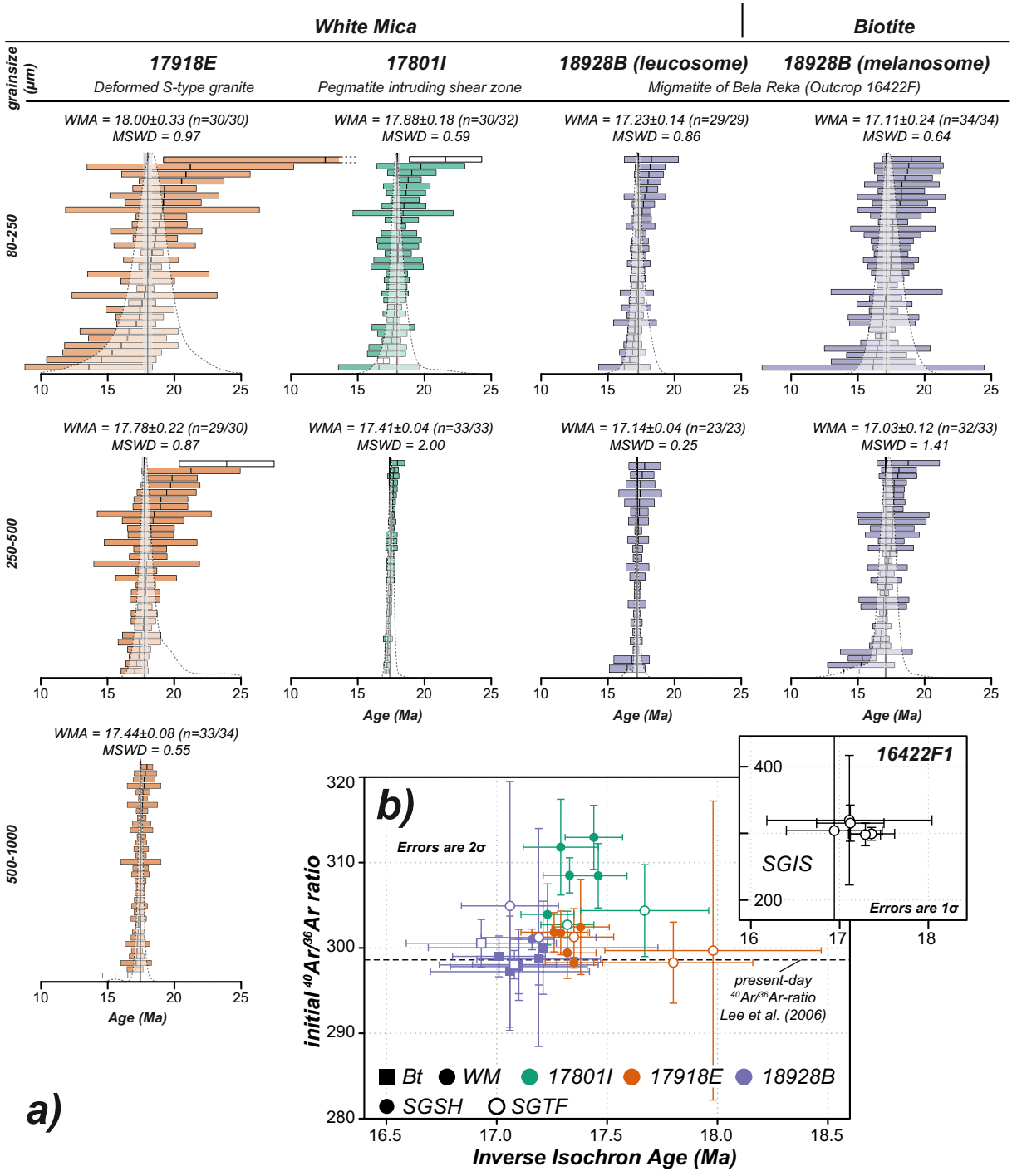

Figure 11. (a) Rank order plots of single-grain total fusion ages obtained on white mica and biotite for different grain sizes. WMA, weighted mean age (confidence interval = 95%, corresponding to 1.96σ); MSWD, mean square of weighted deviates. Empty bars are outlier which was excluded from the calculation of the weighted mean ages. Dashed curves show the corresponding Kernel density estimates. (b) Initial $^{40}Ar/^{36}Ar$-ratios of single-grain total fusion (SGTF; same data as in [a], inverse isochron plots in Figure S1) and single-grain step-heating experiments (SGSH; Figure S2). Inset: same plot type as (b), but for single-grain in situ measurements (SGIS) of 5 WM grains.

10.1029/2021TC006699

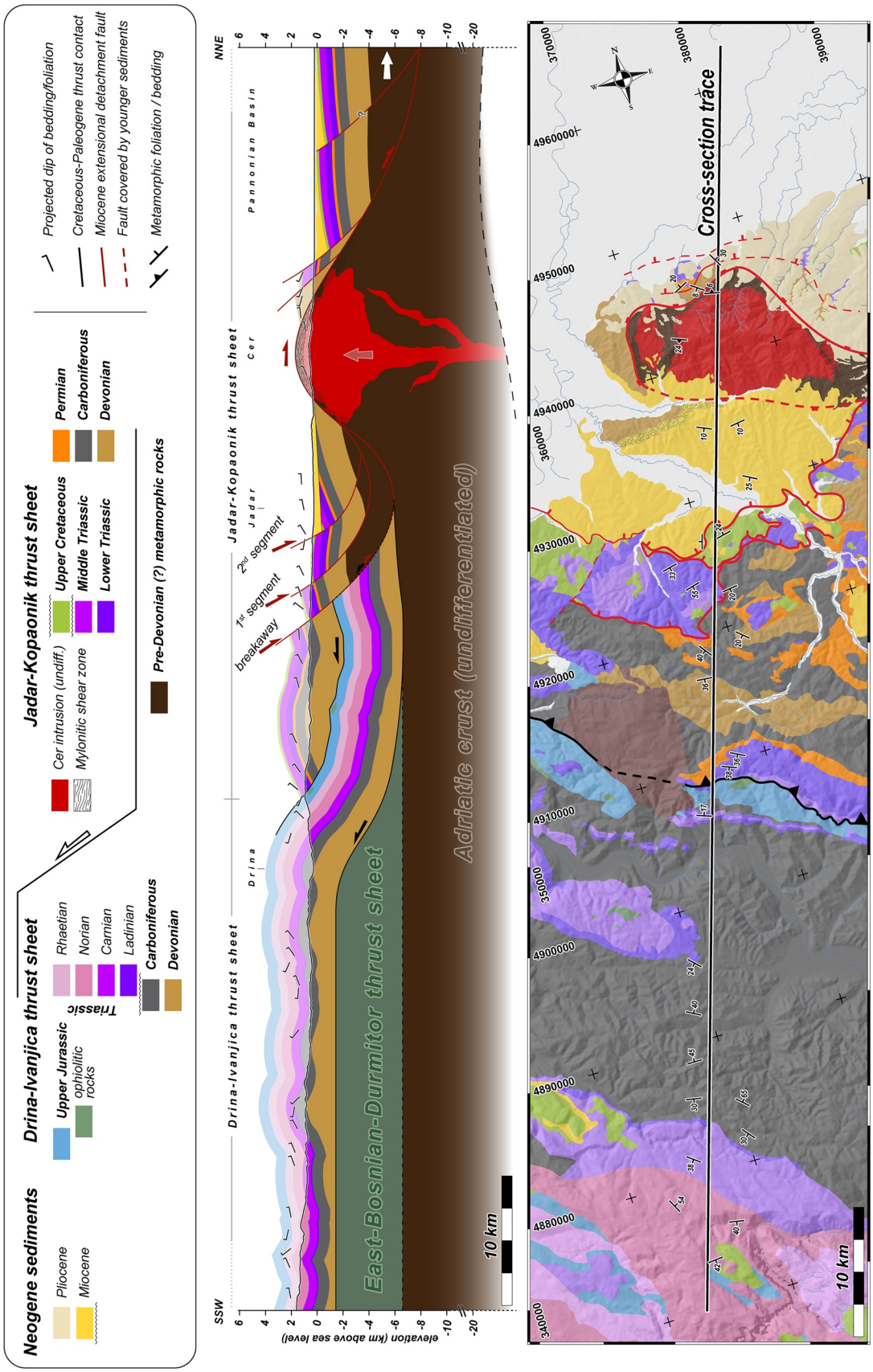

Figure 12. Balanced cross-section through the Cer metamorphic core complex (MCC) and the southerly adjacent nappe contact between the Jadar-Kopaonik thrust sheet in the north and the Drina-Ivanjica composite nappe in the south. Upper Jurassic strata are composed of W-Vardar ophiolites and associated mélange. The breakaway fault that roots in the low-angle extensional shear zone bordering the Cer MCC reactivates the ramp-segment of the nappe contact.

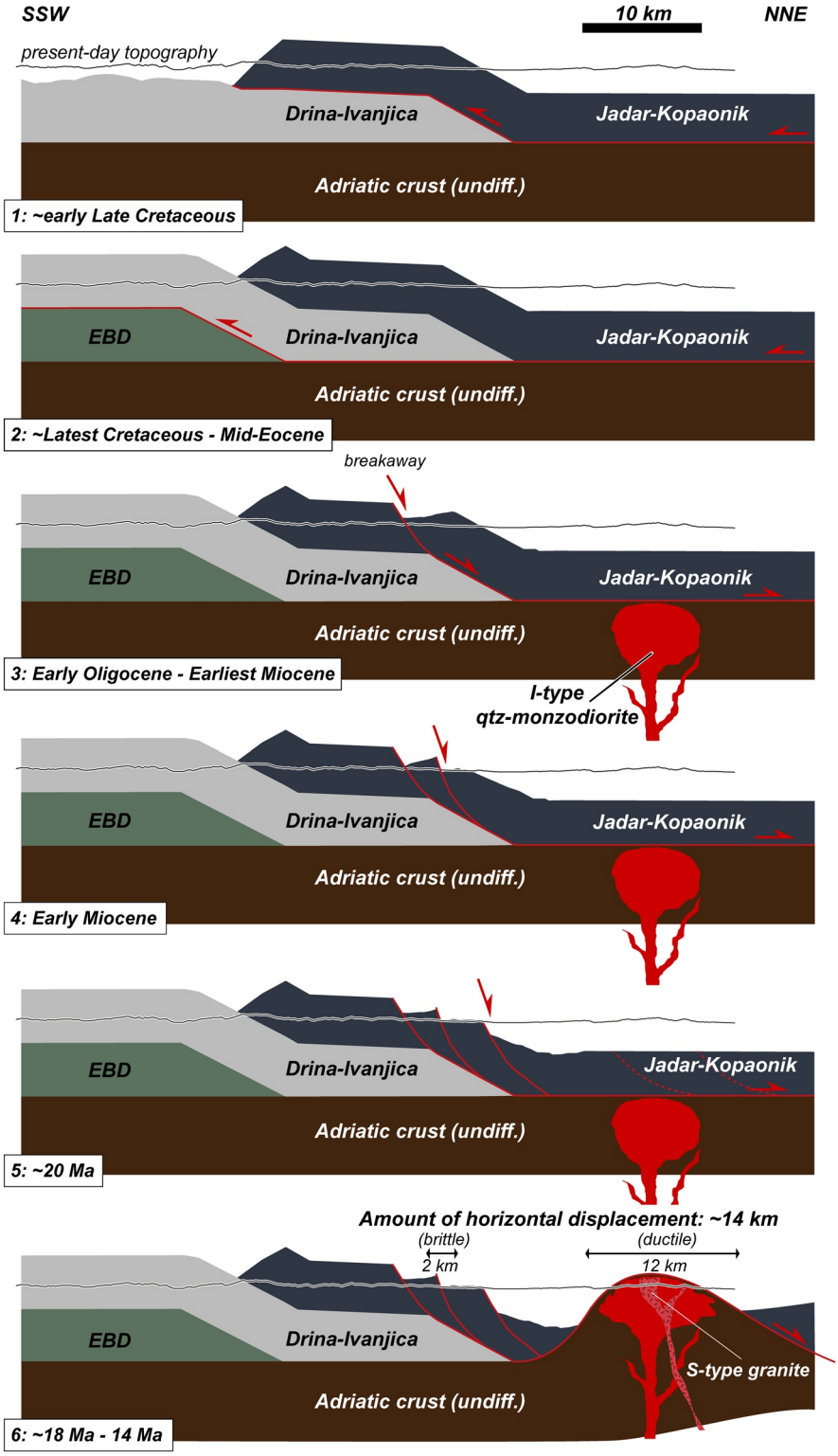

Figure 13. Conceptual kinematic model along an SSW-NNE-oriented transect, illustrating the evolution of the most internal part of the Dinarides since early Late Cretaceous times, post-dating the obduction of the western Vardar ophiolites. These ophiolites are considered the uppermost part of the respective thrust sheets. Red arrows and lines depict areas of active deformation; black lines those of inactive deformation. (1) Thrusting of Jadar-Kopaonik unit onto Drina-Ivanjica (DI) unit. (2) In-sequence thrusting of DI onto the East Bosnian-Durmitor (EBD) unit. (3) Emplacement of I-type intrusion at ~32 Ma. Early Miocene onset of extension (Pannonian Basin peak extension at ~19 Ma, see text) with reactivation of the ramp segment of the former thrust contact as a low-angle normal fault. (4–5) Continuing extension along listric normal faults rooting in a flat detachment along the former thrust plane. (6) Denudation and isostatic uplift of continental crust followed by the intrusion of the S-type granite. Continuing exhumation of Cer MCC.

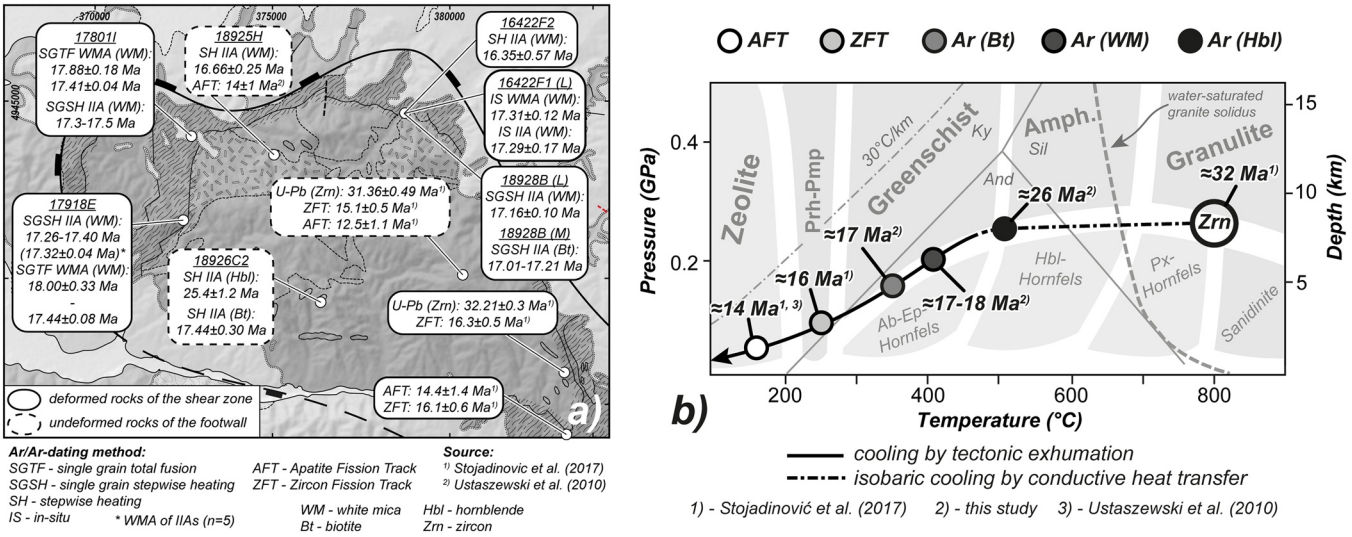

Figure 14. (a) Geochronological data from the Cer massif, own data, and published ones, with data from the shear zone in solid boxes and the undeformed footwall in dashed boxes. WMA, weighted mean age; IIA, inverse isochron age; L, leucosome; M, melanosome. (b) Interpretative P-T-t path of the Cer Massif and surrounding metamorphic rocks. Intrusion of the I-type granitoid at ~32 Ma is followed by isobaric cooling until (c) 20 Ma and final cooling by tectonic denudation.

as the driving force for Middle Miocene extension (Matenco & Radivojević, 2012) is rather likely to have happened in Oligocene times instead, as it pre-dates large-scale N(NE)-S(SW) Early Miocene extension in the internal Dinarides, which we consider to be linked to the rollback of European lithosphere underneath the Carpathians.

6. Conclusions

Our results show that the opening of the Pannonian Basin in response to slab-retreat underneath the Carpathian orogen also affected the Dinarides. The extension was most pronounced in the internal Dinarides and involved the reactivation of former suturing thrusts of the Sava zone as low-angle detachments, shown by Ustaszewski et al. (2010). We now show evidence that Miocene extension in the Pannonian Basin also affected the distal Adriatic margin, where the reactivation of nappe contacts as low-angle detachment systems resulted in the exhumation of mid-crustal core complexes such as Cer MCC at ~17–18 Ma. A possible slab detaching from the Adriatic plate with subsequent mantle delamination can be ruled out as the driving factor, as it pre-dates early Miocene extension.

We demonstrated the applicability of multi-technique $^{40}Ar/^{39}Ar$ geochronology to decipher the activity of a ductile shear zone and its footwall by means of differences in the respective ages. The single-grain total fusion technique is a valuable tool to differentiate several mineral growth generations, as long as processes that mobilize Ar, leading either to Ar-loss or to excess-Ar, can be ruled out. In the case of samples, where these processes cannot be excluded, it is advised to use step heating on single grains rather than on "conventional" mineral concentrates to obtain more reliable age information, or—alternatively—the in situ approach. Our SGTF results showed no evidence for several mica generations in the deformed rocks of the shear zone, meaning that step heating ages of these rocks are reliable.

Data Availability Statement

All data sets compiled for this study as well as the supplementary material can be accessed at https://zenodo.org/record/4678734.

Acknowledgments
We thank our colleagues Ana Mladenović (University Beograd), Dejan Prelević (University Beograd, University Mainz), and Tobias Stephan (University Erlangen-Nürnberg, now at University of Calgary) for their support and in-depth discussions on various subjects regarding structural geology and igneous petrology during joint field work. Gordon Lister (ANU Canberra) is thanked especially for his input during cross-section construction and core-complex-related discussions. We gratefully acknowledge Federico Rossetti, Jan Wijbrans, and Claudio Rosenberg for their constructive and helpful comments that further improved this contribution.

References

Andrić, N., Fügenschuh, B., Životić, D., & Cvetković, V. (2015). The thermal history of the Miocene Ibar Basin (Southern Serbia): New constraints from apatite and zircon fission track and vitrinite reflectance data. *Geologica Carpathica*, *66*(1), 37–50.

Andrić, N., Sant, K., Matenco, L., Mandic, O., Tomljenović, B., Pavelić, D., et al. (2017). The link between tectonics and sedimentation in asymmetric extensional basins: Inferences from the study of the Sarajevo-Zenica Basin. *Marine and Petroleum Geology*, *83*, 305–332.

Bada, G., Horváth, F., Gerner, P., & Fejes, I. (1999). Review of the present-day geodynamics of the Pannonian basin: Progress and problems. *Journal of Geodynamics*, *27*(4-5), 501–527. http://dx.doi.org/10.1016/s0264-3707(98)00013-1

Balázs, A., Matenco, L., Magyar, I., Horváth, F., & Cloetingh, S. (2016). The link between tectonics and sedimentation in back-arc basins: New genetic constraints from the analysis of the Pannonian Basin. *Tectonics*, *35*(6), 1526–1559. https://doi.org/10.1002/2015tc004109

Balla, Z. (1987). Tertiary paleomagnetic data for the Carpatho-Pannonian region in the light of Miocene rotation kinematics. *Tectonophysics*, *139*(1–2), 67–98. https://doi.org/10.1016/0040-1951(87)90198-3

Balling, P., Grützner, C., Tomljenović, B., Spakman, W., & Ustaszewski, K. (2021). Post-collisional mantle delamination in the Dinarides implied from staircases of Oligo-Miocene uplifted marine terraces. *Scientific Reports*, *11*(1), 2685. https://doi.org/10.1038/s41598-021-81561-5

Block, L., & Royden, L. H. (1990). Core complex geometries and regional scale flow in the lower crust. *Tectonics*, *9*(4), 557–567. https://doi.org/10.1029/tc009i004p00557

Brković, T., Malešević, M., Klisić, M., Urošević, M., Trifunović, S., & Radovanović, Z. (1977). Sheet Čačak, Belgrade: Institute for Geological and Geophysical Research. *Basic Geological Map of Former Yugoslavia*, *1*, 100000.

Busch, J. P., Mezger, K., & van der Pluijm, B. A. (1997). Suturing and extensional reactivation in the Grenville orogen, Canada. *Geology*, *25*(6), 507–510. https://doi.org/10.1130/0091-7613(1997)025<0507:saerit>2.3.co;2

Casale, G., Bennett, R., Cowan, D., & Surkovic, M., (2013). Syn-convergence extension and mid-crustal exhumation in the Internal Dinarides.

Cvetković, V., Poli, G., Christofides, G., Koroneos, A., Pécskay, Z., Resimić-Šarić, K., & Erić, V. (2007). The Miocene granitoid rocks of Mt. Bukulja (central Serbia): Evidence for Pannonian extension-related granitoid magmatism in the northern Dinarides. *European Journal of Mineralogy*, *19*(4), 513–532.

Davis, G. A., Anderson, J. L., Frost, E. G., Shackelford, T. J., Crittenden, M. D., Jr, Coney, P. J., & Davis, G. H. (1980). Mylonitization and detachment faulting in the Whipple-Buckskin-Rawhide Mountains terrane, southeastern California and western Arizona, In *Cordilleran metamorphic core complexes*. Geological Society of America.

Davis, G. H., & Coney, P. J. (1979). Geologic development of the Cordilleran metamorphic core complexes. *Geology*, *7*(3), 120–124. https://doi.org/10.1130/0091-7613(1979)7<120:gdotcm>2.0.co;2

Dodson, M. H. (1973). Closure temperature in cooling geochronological and petrological systems. *Contributions to Mineralogy and Petrology*, *40*(3), 259–274. https://doi.org/10.1007/bf00373790

Dovenyi, P., & Horváth, F. (1988). A Review of Temperature, Thermal Conductivity, and Heat Flow Data for the Pannonian Basin: Chapter 16, AAPG Special Volumes. *The Pannonian Basin: A Study in Basin Evolution*, 195–233.

Egan, S., Buddin, T., Kane, S., & Williams, G. (1997). Three-dimensional modeling and visualisation in structural geology: New techniques for the restoration and balancing of volumes. *Paper presented at the Proceedings of the 1996 Geoscience Information Group Conference on Geological Visualisation*. Electronic Geology Special Volume.

Erak, D., Matenco, L., Toljić, M., Stojadinović, U., Andriessen, P. A. M., Willingshofer, E., & Ducea, M. N. (2017). From nappe stacking to extensional detachments at the contact between the Carpathians and Dinarides - The Jastrebac Mountains of Central Serbia. *Tectonophysics*, *710–711*, 162–183. https://doi.org/10.1016/j.tecto.2016.12.022

Filipović, I. (1971). *Basic geological map sheet of Yugoslavia scale 1: 100.000, sheet Vladimirci L34–124*. Federal Geological Institute of Yugoslavia.

Filipović, I., Jovanović, D., Sudar, M., Pelikán, P., Kovács, S., Less, G., & Hips, K. (2003). Comparison of the Variscan–Early Alpine evolution of the Jadar Block (NW Serbia) and "Bükkium"(NE Hungary) terranes; some paleogeographic implications. *Slovak Geological Magazine*, *9*(1), 23–40.

Fodor, L., Csontos, L., Bada, G., Györfi, I., & Benkovics, L. (1999). Tertiary tectonic evolution of the Pannonian Basin system and neighboring orogens: A new synthesis of palaeostress data. *Geological Society, London, Special Publications*, *156*(1), 295–334. https://doi.org/10.1144/gsl.sp.1999.156.01.15

Fodor, L. I., Márton, E., Vrabec, M., Koroknai, B., Trajanova, M., & Vrabec, M. (2020). Relationship between magnetic fabrics and deformation of the Miocene Pohorje intrusions and surrounding sediments (Eastern Alps). *International Journal of Earth Sciences*, *109*, 1377–1401.

Fossen, H. (1992). The role of extensional tectonics in the Caledonides of south Norway. *Journal of Structural Geology*, *14*(8–9), 1033–1046. https://doi.org/10.1016/0191-8141(92)90034-t

Froitzheim, N., Conti, P. t., & Van Daalen, M. (1997). Late Cretaceous, synorogenic, low-angle normal faulting along the Schlinig fault (Switzerland, Italy, Austria) and its significance for the tectonics of the Eastern Alps. *Tectonophysics*, *280*(3–4), 267–293. https://doi.org/10.1016/s0040-1951(97)00037-1

Gallhofer, D., Quadt, A. V., Peytcheva, I., Schmid, S. M., & Heinrich, C. A. (2015). Tectonic, magmatic, and metallogenic evolution of the Late Cretaceous arc in the Carpathian-Balkan orogen. *Tectonics*, *34*(9), 1813–1836. https://doi.org/10.1002/2015tc003834

Gallhofer, D., von Quadt, A., Schmid, S. M., Guillong, M., Peytcheva, I., & Seghedi, I. (2017). Magmatic and tectonic history of Jurassic ophiolites and associated granitoids from the South Apuseni Mountains (Romania). *Swiss Journal of Geosciences*, *110*(2), 699–719. https://doi.org/10.1007/s00015-016-0231-6

Gawlick, H.-J., & Missoni, S. (2019). Middle-Late Jurassic sedimentary mélange formation related to ophiolite obduction in the Alpine-Carpathian-Dinaridic Mountain Range. *Gondwana Research*, *74*, 144–172. https://doi.org/10.1016/j.gr.2019.03.003

Gibbs, A. D. (1983). Balanced cross-section construction from seismic sections in areas of extensional tectonics. *Journal of Structural Geology*, *5*(2), 153–160. https://doi.org/10.1016/0191-8141(83)90040-8

Grove, M., & Harrison, T. M. (1996). ^{40}Ar* diffusion in Fe-rich biotite. *American Mineralogist*, *81*(7–8), 940. https://doi.org/10.2138/am-1996-7-816

Haas, J., & Péró, C. (2004). Mesozoic evolution of the Tisza Mega-unit. *International Journal of Earth Sciences*, *93*(2), 297–313.

Handy, M. R., Ustaszewski, K., & Kissling, E. (2015). Reconstructing the Alps-Carpathians-Dinarides as a key to understanding switches in subduction polarity, slab gaps and surface motion. *International Journal of Earth Sciences*, *104*(1), 1–26. https://doi.org/10.1007/s00531-014-1060-3

Harrison, T. M. (1982). Diffusion of ^{40}Ar in hornblende. *Contributions to Mineralogy and Petrology*, *78*(3), 324–331.
Harrison, T. M., Célérier, J., Aikman, A. B., Hermann, J., & Heizler, M. T. (2009). Diffusion of ^{40}Ar in muscovite. *Geochimica et Cosmochimica Acta*, *73*(4), 1039–1051. https://doi.org/10.1016/j.gca.2008.09.038
Harzhauser, M., & Piller, W. E. (2007). Benchmark data of a changing sea—Paleogeography, paleobiogeography and events in the Central Paratethys during the Miocene, Paleogeography. *Paleogeography, Palaeoclimatology, Palaeoecology*, *253*(1–2), 8–31. https://doi.org/10.1016/j.palaeo.2007.03.031
Horváth, F. (1993). Toward a mechanical model for the formation of the Pannonian basin. *Tectonophysics*, *226*(1–4), 333–357. https://doi.org/10.1016/0040-1951(93)90126-5
Horváth, F., Bada, G., Szafián, P., Tari, G., Ádám, A., & Cloetingh, S. (2006). Formation and deformation of the Pannonian Basin: Constraints from observational data. *Geological Society, London, Memoirs*, *32*(1), 191–206. https://doi.org/10.1144/gsl.mem.2006.032.01.11
Horvath, F. & Berckhemer, H, (1982). Mediterranean Backarc Basins, in *Alpine-mediterranean geodynamics*, (pp. 141–173. https://doi.org/10.1029/gd007p0141
Horváth, F., Musitz, B., Balázs, A., Végh, A., Uhrin, A., Nádor, A., et al. (2015). Evolution of the Pannonian basin and its geothermal resources. *Geothermics*, *53*, 328–352. https://doi.org/10.1016/j.geothermics.2014.07.009
Jolivet, L., Lecomte, E., Huet, B., Denèle, Y., Lacombe, O., Labrousse, L., et al. (2010). The north cycladic detachment system. *Earth and Planetary Science Letters*, *289*(1–2), 87–104. https://doi.org/10.1016/j.epsl.2009.10.032
Kelley, S. (2002). Excess argon in K–Ar and Ar–Ar geochronology. *Chemical Geology*, *188*(1–2), 1–22. https://doi.org/10.1016/s0009-2541(02)00064-5
Knežević, V., Karamata, S., Cvetković, V., & Pécskay, Z. (1994). Genetic groups of the enclaves in the granitic rocks of the Cer Mountain (western Serbia). *Annales Geologiques de la Peninsule Balkanique*, *58*, 219–234.
Knezevic, V., Karamata, S., & Cvetkovic, V. (1994). Tertiary granitic rocks along the southern margin of the Pannonian Basin. *Acta Mineralogica-Petrolographica*, *35*, 71–80.
Koroneos, A., Poli, G., Cvetković, V., Christofides, G., Krstić, D., & Pécskay, Z. (2011). Petrogenetic and tectonic inferences from the study of the Mt Cer pluton (West Serbia). *Geological Magazine*, *148*(1), 89–111. https://doi.org/10.1017/s0016756810000476
Kossmat, F. (1924). *Geologie der zentralen Balkanhalbinsel: Mit einer Übersicht des dinarischen Gebirgsbaus*. Gebr. Borntraeger.
Kuiper, Y. D. (2002). The interpretation of inverse isochron diagrams in ^{40}Ar/^{39}Ar geochronology. *Earth and Planetary Science Letters*, *203*(1), 499–506. https://doi.org/10.1016/s0012-821x(02)00833-6
Lee, J. K. W. (1995). Multipath diffusion in geochronology. *Contributions to Mineralogy and Petrology*, *120*(1), 60–82. https://doi.org/10.1007/s004100050058
Lee, J.-Y., Marti, K., Severinghaus, J. P., Kawamura, K., Yoo, H.-S., Lee, J. B., & Kim, J. S. (2006). A redetermination of the isotopic abundances of atmospheric Ar. *Geochimica et Cosmochimica Acta*, *70*(17), 4507–4512. https://doi.org/10.1016/j.gca.2006.06.1563
Lister, G. S., & Baldwin, S. L. (1993). Plutonism and the origin of metamorphic core complexes. *Geology*, *21*(7), 607–610. https://doi.org/10.1130/0091-7613(1993)021<0607:patoom>2.3.co;2
Lister, G. S., Banga, G., & Feenstra, A. (1984). Metamorphic core complexes of Cordilleran type in the Cyclades, Aegean Sea, Greece. *Geology*, *12*(4), 221–225. https://doi.org/10.1130/0091-7613(1984)12<221:mccoct>2.0.co;2
Lister, G. S., & Davis, G. A. (1989). The origin of metamorphic core complexes and detachment faults formed during Tertiary continental extension in the northern Colorado River region, U.S.A. *Journal of Structural Geology*, *11*, 65–94. https://doi.org/10.1016/0191-8141(89)90036-9
Malinverno, A., & Ryan, W. B. F. (1986). Extension in the Tyrrhenian Sea and shortening in the Apennines as result of arc migration driven by sinking of the lithosphere. *Tectonics*, *5*(2), 227–245. https://doi.org/10.1029/tc005i002p00227
Matenco, L., & Radivojević, D. (2012). On the formation and evolution of the Pannonian Basin: Constraints derived from the structure of the junction area between the Carpathians and Dinarides, Tectonics. *31*(6).
Mojsilović, S., Filipović, I., Rodin, V., Navala, M., Baklaić, D., & Djoković, I. (1975). Federal Geological Institute of Yugoslavia, Beograd. *Basic geological map sheet of Yugoslavia scale*, *1*, 100.
Nemcok, M., Pospisil, L., Lexa, J., & Donelick, R. (1998). Tertiary subduction and slab break-off model of the Carpathian–Pannonian region. *Tectonophysics*, *295*(3–4), 307–340. https://doi.org/10.1016/s0040-1951(98)00092-4
Nirta, G., Aberhan, M., Bortolotti, V., Carras, N., Menna, F., & Fazzuoli, M. (2020). Deciphering the geodynamic evolution of the Dinaric orogen through the study of the 'overstepping' Cretaceous successions. *Geological Magazine*, *157*(8), 1238–1264. https://doi.org/10.1017/s001675682000045x
Pamić, J. (1993). Eoalpine to Neoalpine magmatic and metamorphic processes in the northwestern Vardar Zone, the easternmost Periadriatic Zone and the southwestern Pannonian Basin. *Tectonophysics*, *226*(1–4), 503–518.
Pamic, J., Balen, D., & Herak, M. (2002). Origin and geodynamic evolution of Late Paleogene magmatic associations along the Periadriatic-Sava-Vardar magmatic belt. *Geodinamica Acta*, *15*(4), 209–231. https://doi.org/10.1016/s0985-3111(02)01089-6
Pfänder, J. A., Sperner, B., Ratschbacher, L., Fischer, A., Meyer, M., Leistner, M., & Schaeben, H. (2014). High-resolution ^{40}Ar/^{39}Ar dating using a mechanical sample transfer system combined with a high-temperature cell for step heating experiments and a multicollector ARGUS noble gas mass spectrometer. *Geochemistry, Geophysics, Geosystems*, *15*(6), 2713–2726. https://doi.org/10.1002/2014gc005289
Platt, J. P., Behr, W. M., & Cooper, F. J. (2015). Metamorphic core complexes: Windows into the mechanics and rheology of the crust. *Journal of the Geological Society*, *172*(1), 9–27. https://doi.org/10.1144/jgs2014-036
Porkoláb, K., Kövér, S., Benkó, Z., Héja, G. H., Fialowski, M., Soós, B., et al. (2019). Structural and geochronological constraints from the Drina-Ivanjica thrust sheet (Western Serbia): Implications for the Cretaceous-Paleogene tectonics of the Internal Dinarides. *Swiss Journal of Geosciences*, *112*(1), 217–234. https://doi.org/10.1007/s00015-018-0327-2
Prelević, D., Foley, S., Romer, R., Cvetković, V., & Downes, H. (2005). Tertiary ultrapotassic volcanism in Serbia: Constraints on petrogenesis and mantle source characteristics. *Journal of Petrology*, *46*(7), 1443–1487.
Rabillard, A., Jolivet, L., Arbaret, L., Bessière, E., Laurent, V., Menant, A., et al. (2018). Synextensional granitoids and detachment systems within cycladic metamorphic core complexes (Aegean Sea, Greece): Toward a regional tectonomagmatic model. *Tectonics*, *37*(8), 2328–2362. https://doi.org/10.1029/2017tc004697
Rajčević, D. N. (1982). *Osnovna geološka karta SFRJ, List Šabac L34-112-razmera 1: 100 000 (Basic geological map of Yugoslavia, sheet Šabac)*. Federal Geological Survey.
Ratschbacher, L., Merle, O., Davy, P., & Cobbold, P. (1991). Lateral extrusion in the Eastern Alps, part 1: Boundary conditions and experiments scaled for gravity. *Tectonics*, *10*(2), 245–256. https://doi.org/10.1029/90tc02622

Renne, P. R., Mundil, R., Balco, G., Min, K., & Ludwig, K. R. (2010). Joint determination of ^{40}K decay constants and ^{40}Ar*/^{40}K for the Fish Canyon sanidine standard, and improved accuracy for ^{40}Ar/^{39}Ar geochronology. *Geochimica et Cosmochimica Acta*, *74*(18), 5349–5367. https://doi.org/10.1016/j.gca.2010.06.017

Reynolds, S. J., & Lister, G. S. (1990). Folding of mylonitic zones in Cordilleran metamorphic core complexes: Evidence from near the mylonitic front. *Geology*, *18*(3), 216–219. https://doi.org/10.1130/0091-7613(1990)018<0216:fomzic>2.3.co;2

Ridolfi, F., & Renzulli, A. (2012). Calcic amphiboles in calc-alkaline and alkaline magmas: Thermobarometric and chemometric empirical equations valid up to 1,130°C and 2.2 GPa. *Contributions to Mineralogy and Petrology*, *163*(5), 877–895. https://doi.org/10.1007/s00410-011-0704-6

Robertson, A., Karamata, S., & Šarić, K. (2009). Overview of ophiolites and related units in the Late Palaeozoic–Early Cenozoic magmatic and tectonic development of Tethys in the northern part of the Balkan region. *Lithos*, *108*(1–4), 1–36. https://doi.org/10.1016/j.lithos.2008.09.007

Rosenberg, C. L., Brun, J.-P., & Gapais, D. (2004). Indentation model of the Eastern Alps and the origin of the Tauern Window. *Geology*, *32*(11), 997–1000. https://doi.org/10.1130/g20793.1

Royden, L., (1988). *Late Cenozoic Tectonics of the Pannonian Basin System: Chapter 3*. https://doi.org/10.1306/m45474c3

Royden, L., Horváth, F., Nagymarosy, A., & Stegena, L. (1983). Evolution of the Pannonian basin system: 2. Subsidence and thermal history. *Tectonics*, *2*(1), 91–137. https://doi.org/10.1029/tc002i001p00091

Sant, K., Andrić, N., Mandic, O., Demir, V., Pavelić, D., Rundić, L., et al. (2018). Magneto-biostratigraphy and paleoenvironments of the Miocene freshwater sediments of the Sarajevo-Zenica Basin. *Palaeogeography, Palaeoclimatology, Palaeoecology*, *506*, 48–69. https://doi.org/10.1016/j.palaeo.2018.06.009

Schaen, A. J., Jicha, B. R., Hodges, K. V., Vermeesch, P., Stelten, M. E., Mercer, C. M., et al. (2020). Interpreting and reporting ^{40}Ar/^{39}Ar geochronologic data. *GSA Bulletin, 133*(3-4), 461–487.

Schefer, S., Cvetković, V., Fügenschuh, B., Kounov, A., Ovtcharova, M., Schaltegger, U., & Schmid, S. M. (2011). Cenozoic granitoids in the Dinarides of southern Serbia: Age of intrusion, isotope geochemistry, exhumation history and significance for the geodynamic evolution of the Balkan Peninsula. *International Journal of Earth Sciences*, *100*(5), 1181–1206. https://doi.org/10.1007/s00531-010-0599-x

Schefer, S., Egli, D., Missoni, S., Bernoulli, D., Fügenschuh, B., Gawlick, H.-J., et al. (2010). Triassic metasediments in the internal Dinarides (Kopaonik area, southern Serbia): Stratigraphy, paleogeographic and tectonic significance. *Geologica Carpathica*, *61*(2), 89–109. http://dx.doi.org/10.2478/v10096-010-0003-6

Schmid, S. M., Bernoulli, D., Fügenschuh, B., Matenco, L., Schefer, S., Schuster, R., et al. (2008). The Alpine-Carpathian-Dinaridic orogenic system: Correlation and evolution of tectonic units. *Swiss Journal of Geosciences*, *101*(1), 139–183. https://doi.org/10.1007/s00015-008-1247-3

Schmid, S. M., Fügenschuh, B., Kounov, A., Maţenco, L., Nievergelt, P., Oberhänsli, R., et al. (2020). Tectonic units of the Alpine collision zone between Eastern Alps and western Turkey. *Gondwana Research*, *78*, 308–374. https://doi.org/10.1016/j.gr.2019.07.005

Schneider, S., Hammerschmidt, K., & Rosenberg, C. L. (2013). Dating the longevity of ductile shear zones: Insight from ^{40}Ar/^{39}Ar in situ analyses. *Earth and Planetary Science Letters*, *369–370*, 43–58. https://doi.org/10.1016/j.epsl.2013.03.002

Schwarz, W. H., & Trieloff, M. (2007). Intercalibration of ^{40}Ar/^{39}Ar age standards NL-25, HB3gr hornblende, GA1550, SB-3, HD-B1 biotite and BMus/2 muscovite. *Chemical Geology*, *242*(1–2), 218–231. https://doi.org/10.1016/j.chemgeo.2007.03.016

Sperner, B., Ratschbacher, L., & Nemčok, M. (2002). Interplay between subduction retreat and lateral extrusion: Tectonics of the Western Carpathians. *Tectonics*, *21*(6), 11–124. https://doi.org/10.1029/2001tc901028

Stipp, M., Stünitz, H., Heilbronner, R., & Schmid, S. M. (2002a). Dynamic recrystallization of quartz: Correlation between natural and experimental conditions. *Geological Society, London, Special Publications*, *200*(1), 171–190. https://doi.org/10.1144/gsl.sp.2001.200.01.11

Stipp, M., Stünitz, H., Heilbronner, R., & Schmid, S. M. (2002b). The eastern Tonale fault zone: A 'natural laboratory' for crystal plastic deformation of quartz over a temperature range from 250 to 700°C. *Journal of Structural Geology*, *24*(12), 1861–1884. https://doi.org/10.1016/s0191-8141(02)00035-4

Stojadinovic, U., Matenco, L., Andriessen, P. A. M., Toljić, M., & Foeken, J. P. T. (2013). The balance between orogenic building and subsequent extension during the Tertiary evolution of the NE Dinarides: Constraints from low-temperature thermochronology. *Global and Planetary Change*, *103*, 19–38. https://doi.org/10.1016/j.gloplacha.2012.08.004

Stojadinovic, U., Matenco, L., Andriessen, P., Toljić, M., Rundić, L., & Ducea, M. N. (2017). Structure and provenance of Late Cretaceous-Miocene sediments located near the NE Dinarides margin: Inferences from kinematics of orogenic building and subsequent extensional collapse. *Tectonophysics*, *710–711*, 184–204. https://doi.org/10.1016/j.tecto.2016.12.021

Subašić, S., Prevolnik, S., Herak, D., & Herak, M. (2017). Observations of SKS splitting beneath the Central and Southern External Dinarides in the Adria-Eurasia convergence zone. *Tectonophysics*, *705*, 93–100.

Suppe, J. (1983). Geometry and kinematics of fault-bend folding. *American Journal of Science*, *283*(7), 684–721. https://doi.org/10.2475/ajs.283.7.684

Tari, G., Dövényi, P., Dunkl, I., Horváth, F., Lenkey, L., Stefanescu, M., et al. (1999). Lithospheric structure of the Pannonian basin derived from seismic, gravity and geothermal data. *Geological Society, London, Special Publications*, *156*(1), 215–250. https://doi.org/10.1144/gsl.sp.1999.156.01.12

Tari, G., Horváth, F., & Rumpler, J. (1992). Styles of extension in the Pannonian Basin. *Tectonophysics*, *208*(1–3), 203–219. https://doi.org/10.1016/0040-1951(92)90345-7

Tari, V., & Pamić, J. (1998). Geodynamic evolution of the northern Dinarides and the southern part of the Pannonian Basin. *Tectonophysics*, *297*(1–4), 269–281. https://doi.org/10.1016/s0040-1951(98)00172-3

Toljić, M., Matenco, L., Ducea, M. N., Stojadinović, U., Milivojević, J., & Đerić, N. (2013). The evolution of a key segment in the Europe–Adria collision: The Fruška Gora of northern Serbia. *Global and Planetary Change*, *103*, 39–62.

Tomek, Č., & Hall, J. (1993). Subducted continental margin imaged in the Carpathians of Czechoslovakia. *Geology*, *21*(6), 535–538. https://doi.org/10.1130/0091-7613(1993)021<0535:scmiin>2.3.co;2

Ustaszewski, K., Kounov, A., Schmid, S. M., Schaltegger, U., Krenn, E., Frank, W., & Fügenschuh, B. (2010). Evolution of the Adria-Europe plate boundary in the northern Dinarides: From continent-continent collision to back-arc extension. *Tectonics*, *29*(6).

Ustaszewski, K., Schmid, S. M., Lugović, B., Schuster, R., Schaltegger, U., Bernoulli, D., et al. (2009). Late Cretaceous intra-oceanic magmatism in the internal Dinarides (northern Bosnia and Herzegovina): Implications for the collision of the Adriatic and European plates. *Lithos*, *108*(1–4), 106–125. https://doi.org/10.1016/j.lithos.2008.09.010

Uunk, B., Brouwer, F., ter Voorde, M., & Wijbrans, J. (2018). Understanding phengite argon closure using single grain fusion age distributions in the Cycladic Blueschist Unit on Syros, Greece. *Earth and Planetary Science Letters*, *484*, 192–203. https://doi.org/10.1016/j.epsl.2017.12.031

Uyeda, S., & Kanamori, H. (1979). Back-arc opening and the mode of subduction. *Journal of Geophysical Research*, *84*(B3), 1049–1061. https://doi.org/10.1029/jb084ib03p01049

Van Unen, M., Matenco, L., Nader, F. H., Darnault, R., Mandic, O., & Demir, V. (2019). Kinematics of foreland-vergent crustal accretion: Inferences from the Dinarides evolution. *Tectonics*, *38*(1), 49–76. https://doi.org/10.1029/2018tc005066

Vermeesch, P. (2018). IsoplotR: A free and open toolbox for geochronology. *Geoscience Frontiers*, *9*(5), 1479–1493. https://doi.org/10.1016/j.gsf.2018.04.001

Vlahović, I., Tišljar, J., Velić, I., & Matičec, D. (2005). Evolution of the Adriatic carbonate platform: Paleogeography, main events and depositional dynamics. *Paleogeography, Palaeoclimatology, Palaeoecology*, *220*(3–4), 333–360.

Vrhovčić, J., Mojičević, M., Anđelković, I., Marković, B., Pavlović, Z., Rajčević, D., et al. (1984). *Osnovna geološka karta SFRJ, List Bijeljina L34-111-razmera 1: 100 000 (Basic geological map of Yugoslavia, sheet Bijeljina*. Federal Geologal Survey.

Wernicke, B. (1985). Uniform-sense normal simple shear of the continental lithosphere. *Canadian Journal of Earth Sciences*, *22*(1), 108–125. https://doi.org/10.1139/e85-009

Wijbrans, J. R., Schliestedt, M., & York, D. (1990). Single grain argon laser probe dating of phengites from the blueschist to greenschist transition on Sifnos (Cyclades, Greece). *Contributions to Mineralogy and Petrology*, *104*(5), 582–593. https://doi.org/10.1007/bf00306666

Withjack, M. O., & Peterson, E. T. (1993). Prediction of normal-fault geometries—A sensitivity analysis. *AAPG Bulletin*, *77*(11), 1860–1873.

References From the Supporting Information

Sperner, B., Jonckheere, R., & Pfänder, J. A. (2014). Testing the influence of high-voltage mineral liberation on grain size, shape and yield, and on fission track and $^{40}Ar/^{39}Ar$ dating. *Chemical Geology*, *371*, 83–95. https://doi.org/10.1016/j.chemgeo.2014.02.003